

Mid- to Far-IR Emission and Star Formation in Early-Type Galaxies

Lisa M. Young

Physics Department, New Mexico Tech, Socorro, NM 87801

lyoung@physics.nmt.edu

George J. Bendo

*Astrophysics Group, Imperial College London, Blackett Laboratory, Prince Consort Road,
London, W5 2JN, United Kingdom*

Danielle M. Lucero

Physics Department, New Mexico Tech, Socorro, NM 87801

ABSTRACT

Many early-type galaxies have been detected at wavelengths of 24 to 160 μm but the emission is usually dominated by heating from an AGN or from the evolved stellar population. Here we present *Spitzer* MIPS observations of a sample of elliptical and lenticular galaxies that are rich in cold molecular gas, and we investigate whether the MIR to FIR emission could be associated with star formation activity. The 24 μm images show a rich variety of structures, including nuclear point sources, rings, disks, and smooth extended emission. Comparisons to matched-resolution CO and radio continuum images suggest that the bulk of the 24 μm emission can be traced to star formation with some notable exceptions. The 24 μm luminosities of the CO-rich galaxies are typically a factor of 15 larger than what would be expected from the dust associated with their evolved stars. In addition, FIR/radio flux density ratios are consistent with star formation. We conclude that the star formation rates in $z = 0$ elliptical and lenticular galaxies, as inferred by other authors from UV and optical data, are roughly consistent with the molecular gas abundances and that the molecular gas is usually unstable to star formation activity.

Subject headings: galaxies: elliptical and lenticular, cD — galaxies: ISM — galaxies: individual (UGC 1503, NGC 0807, NGC 2320, NGC 3032, NGC 3656, NGC 4459, NGC 4476, NGC 4526, NGC 5666)

1. Introduction

In recent years, UV and optical photometry and spectroscopy of nearby elliptical galaxies has suggested that these galaxies, which have a reputation for being old, red, and dead, may not be

quite as dead as previously assumed. Between a few percent to 30% of local ellipticals appear to be experiencing low levels of ongoing star formation activity (Schawinski et al. 2007a,b; Kaviraj et al. 2007; Fukugitga et al. 2004; Rogers et al. 2007). The star formation is not intense enough to affect the galaxies’ morphological classification, as it only amounts to a few percent of the total stellar mass. However, this disk growth inside spheroidal galaxies may be a faint remnant of a process that was more vigorous in the past and may have played a role in establishing the range of galaxy morphologies we observe today.

Star formation, of course, requires cold gas, so interpreting the UV and optical data in terms of star formation activity has important implications both for the early-type galaxies and for a general understanding of the star formation process. It is not obvious that star formation should “work” the same way inside spheroidal galaxies as it does inside disks, with the same efficiency, the same dependence on the gas surface density, or the same regulatory mechanisms. For example, it has been hypothesized that even if there is a molecular disk inside an elliptical or lenticular galaxy, the disk would probably be stabilized by the galaxy’s steep gravitational potential (Kennicutt 1989; Okuda et al. 2005; Kawata et al. 2007). Thus it is of interest to probe the relationships between molecular gas and star formation activity in early-type galaxies.

It is not as straightforward, however, to measure star formation rates in early-type galaxies as it is in spirals. Nebular line emission is common in ellipticals (Shields 1991; Goudfrooij et al. 1994; Sarzi et al. 2005), but it is usually not thought to be associated with star formation. Its distribution is generally smooth, centrally peaked, and sometimes filamentary (Shields 1991; Macchetto et al. 1996); its morphology and line ratios suggest ionization sources such as AGN activity, evolved stars, or cooling from the hot gas phase rather than star formation. Far-IR (FIR) and cm-wave radio continuum emission are also commonly used as tracers of star formation activity in gas-rich spirals, but AGNs and the evolved stellar population have been identified as the sources of mid-IR (MIR) and FIR emission in most elliptical galaxies (Temi et al. 2007, 2008).

Here we investigate evidence for and against star formation activity in a sample of elliptical and lenticular galaxies that have unusually large molecular gas contents. We make use of matched-resolution images of the molecular gas distribution, the cm-wave radio continuum and the $24\mu\text{m}$ intensity. The properties of more typical, CO-poor early-type galaxies are reviewed so that they can provide a comparison sample for the CO-rich early-type galaxies. We then present the morphology of the $24\mu\text{m}$ emission, with simple parametric fits and comparisons to molecular gas, radio continuum, and optical images that show dust disks in silhouette. The mid-IR and far-IR flux densities of the CO-rich galaxies are presented along with discussion of the $24\mu\text{m}$ to $2\mu\text{m}$ flux density ratios and the FIR/radio flux density ratios as diagnostics of whether the mid- to far-IR emission has a circumstellar or star formation origin. The results are mixed; in some cases it is clear that the $24\mu\text{m}$ emission is primarily associated with star formation, and in other cases heating by the evolved stellar population or even by an AGN are inferred. Thus, the results are at least qualitatively consistent with the suggestions that present-day star formation activity may be occurring in substantial numbers of local early-type galaxies.

2. Context: the Mid- and Far-Infrared Continuum Emission of Early-Type Galaxies

The ISOCAM and ISOPHOT instruments aboard the *Infrared Space Observatory* provided some insight into the variety of processes that contribute to the mid-IR and far-IR emission of early-type galaxies. For example, a handful of elliptical and lenticular galaxies found their way into the *ISO Atlas of Bright Spiral Galaxies* and are discussed by Bendo et al. (2002a,b) with particular reference to the rate and distribution of star formation activity. The $12\mu\text{m}$ images show very little emission beyond their galaxies’ nuclei. In Bendo et al. (2002b), enhanced MIR and FIR to K flux density ratios are used as star formation indicators. It is not at all obvious that this interpretation is accurate for early-type galaxies, but in most of these cases the ratios are consistent with interstellar radiation fields due to the old stellar population so little if any star formation activity is inferred. There are a minority of E-S0/a galaxies whose FIR/ K flux density ratios (within a $15''$ aperture) are as high as the median values for Sb-Scd spirals, suggesting the possibility of star formation activity.

Xilouris et al. (2004) fit the spectral energy distributions (SEDs) and compared $15\mu\text{m}$ images to optical and near-IR images for a sample of 18 ellipticals, dwarf ellipticals, and lenticulars. In two cases they found no evidence for excess $15\mu\text{m}$ emission over the stellar photospheric emission; in most of the rest of the sample there is such an excess and it is smoothly distributed, more or less following the stellar distribution. A few targets show thermal emission at $15\mu\text{m}$ from the dust that is visible in silhouette in the optical images, and two show AGN emission (a nuclear point source and even some synchrotron radiation from the jet in M87). Thus, in early-type galaxies the stellar photospheres, circumstellar dust, silhouette dust lanes or disks, AGN, and (possibly) star formation all contribute in the mid-IR images.

Fourteen galaxies classified as E, S0, or S0/a were observed as part of the Spitzer Infrared Nearby Galaxies Survey (SINGS; Kennicutt et al. 2003). Eleven of these were detected up to $160\mu\text{m}$ and the $24\mu\text{m}$ morphologies of these galaxies are discussed by Bendo et al. (2007). With a couple of exceptions, such as NGC 1316 (which has asymmetric extended emission over $2'$) and NGC 5866 (which contains an edge-on disk), these early-type galaxies tended to have only poorly resolved nuclear emission at $24\mu\text{m}$. Six of the 11 also have published CO observations (Wiklind et al. 1995; Lees et al. 1991; Knapp & Rupen 1996; Welch & Sage 2003), and four of the six are detected. NGC 5866 is notably CO-rich, as a large amount of molecular gas ($4.4 \times 10^8 M_{\odot}$) is very clearly detected by Welch & Sage (2003). However, maps of the molecular gas distributions in most of these galaxies are not currently available.

MIPS observations of more typically CO-poor elliptical galaxies have also been published by Kaneda et al. (2007) and Temi et al. (2007, 2008). Of the 19 galaxies analyzed by Temi et al. (2008), 13 have been searched for CO emission and none have been detected (Combes et al. 2007; Sage, Welch, & Young 2007). Temi et al. (2008) show that the $24\mu\text{m}$ emission from their ellipticals follows the $r^{1/4}$ near-IR surface brightness profiles very closely. The $24\mu\text{m}$ emission even has the same effective radius as in K ; the ratio of two radii is found to be 0.96 with a dispersion of 0.20.

In addition, Temi et al. (2007) have shown that the $24\mu\text{m}$ emission globally tracks the optical luminosity in elliptical galaxies as there is a tight linear correlation between the $24\mu\text{m}$ flux density and the B -band flux density. This $24\mu\text{m}$ emission is interpreted to be circumstellar dust from the mass loss of post main sequence stars.

In short, several processes may contribute to MIR emission from early-type galaxies. In the majority of the elliptical galaxies that are not CO-rich the $24\mu\text{m}$ emission seems to either follow the stellar photospheric emission or a nuclear source. Extended $15\mu\text{m}$ and $24\mu\text{m}$ emission has been observed from a few early-type galaxies that are very rich in molecular gas or that exhibit silhouetted dust. Until now, however, it has been rare to be able to compare the distribution of possible star formation activity in early-type galaxies to that of the molecular gas, the raw material for the star formation.

3. Target Selection, Observations, and Data Reduction

Most early surveys for molecular gas in early-type galaxies were strongly biased towards FIR-bright targets, with a typical selection criterion having an IRAS $100\mu\text{m}$ flux density > 1 Jy (Lees et al. 1991; Wiklind et al. 1995; Knapp & Rupen 1996). More recent CO searches are not FIR-biased, but they still find significant molecular gas contents. Welch & Sage (2003) reached a surprisingly high CO detection rate of 78% in a volume-limited sample of nearby field lenticular galaxies, and Sage, Welch, & Young (2007) detected CO emission in 33% of a similar sample of field ellipticals. Combes et al. (2007) also detected CO emission in 28% of the early-type galaxies in the SAURON survey (de Zeeuw et al. 2002), a representative sample that uniformly fills an optical magnitude – apparent axis ratio space. Thus, the CO detection rates in ellipticals and lenticulars are high enough to support the UV-inferred incidence of star formation activity (if that gas does indeed engage in star formation). The cold gas masses are highly variable in these detections, with M_{gas}/L_B in the range 10^{-1} to 10^{-3} and lower.

Since we are interested in morphology as a means of distinguishing the origin of the MIR, FIR, and radio emission, we have selected for this project some of the relatively few elliptical and lenticular galaxies with maps resolving their molecular gas distribution (Young 2002, 2005; Young et al. 2008). Because of the way galaxies were selected for CO mapping, the targets were already known to be FIR-bright and to have concentrations of molecular gas in their centers (as opposed to their outskirts). We also apply a criterion on the angular extent of the molecular gas to be able to test the correspondence between the molecular gas and $24\mu\text{m}$ emission. If the $24\mu\text{m}$ emission arises in star formation activity, we expect it to trace the molecular gas. If the $24\mu\text{m}$ emission is related to AGN activity, we expect it to be a point source, and if it comes from circumstellar dust, it should trace the stellar distribution. Thus, we required the targets to have molecular gas in structures on the order of $20''$ to $30''$ or more in diameter. Corresponding dust emission, if present, should be resolved in the $24\mu\text{m}$ images. The targets' distances range up to 80 Mpc and optical luminosities are in the range $-21.7 \leq M_B \leq -18.3$ (Table 1).

Observations of UGC 1503, NGC 807, NGC 2320, NGC 3032, NGC 3656, NGC 4476, and NGC 5666 were made with the MIPS instrument at 24, 70, and $160\mu\text{m}$ in project 20780 of cycle GO-2. The data were taken in photometry mode using the large field size in all cases. Relatively short exposures were used to avoid saturation on these bright sources in medium-high background regions. Exposures were made in four cycles of 10 seconds at $24\mu\text{m}$, with sky offsets of $300''$, and in 8 cycles of 3 seconds at $160\mu\text{m}$. Observations at $70\mu\text{m}$ were made in the fixed cluster-offsets mode with offsets $\pm 80''$, and 8 cycles of 3 seconds. To maximize the morphological information recoverable at $70''$ the fine pixel scale was used. However, most sources were not expected to be usefully resolved at $160\mu\text{m}$ so the single pointing (rather than a raster map) was used at the longer wavelength.

Data for NGC 4526 were obtained from GTO project 69 (PI: Fazio). Those observations consist of a 10s exposure at $24\mu\text{m}$ using the small field with a $300''$ sky offset, 3 cycles of 3 seconds at $70\mu\text{m}$ using the default pixel scale and small field, and 3 cycles of 3 seconds at $160\mu\text{m}$ in the default pixel scale in a 3-by-1 raster map. Data for NGC 4459 were obtained from GO project 3649 (PI: Côte); the observing modes are similar to those for NGC 4526 except that the exposure times are 10 cycles of 4 seconds at $24\mu\text{m}$, 10 cycles of 5 seconds at $70\mu\text{m}$, and 10 cycles of 6 seconds at $160\mu\text{m}$.

The 24, 70, and $160\mu\text{m}$ images were created from raw data frames using the MIPS Data Analysis Tools (MIPS DAT; Gordon et al. 2005) version 3.10 along with additional processing steps. The processing steps for the 70 and $160\mu\text{m}$ data are similar, but the steps for the $24\mu\text{m}$ data are significantly different from these other two bands. Therefore, the $24\mu\text{m}$ data processing is described first followed by descriptions of the 70 and $160\mu\text{m}$ data processing.

The individual $24\mu\text{m}$ frames were first processed through a droop correction (removing an excess signal in each pixel that is proportional to the signal in the entire array) and were corrected for non-linearity in the ramps. The dark current was then subtracted. Next, scan-mirror-position dependent flats were created from the data in each Astronomical Observation Request (AOR) and were applied to the data. Detector pixels that had measured signals of 2500 DN s^{-1} in any frame were masked out in the following three frames so as to avoid having latent images appear in the data. Next, a scan-mirror-position independent flat was created from the data in each AOR and were applied to the data. Following this, planes were fit to the zodiacal light emission in the background regions in each frame (regions falling outside the optical disks of the galaxies that also did not contain any other bright sources), and these planes were subtracted from the data. Next, a robust statistical analysis was applied in which the values of cospatial pixels from different frames were compared to each other and statistical outliers (e.g. probable cosmic rays) are masked out. After this, a final mosaic was made with pixel sizes of $1.5''$, any residual background in the image was subtracted, and the data were calibrated into astronomical units. The calibration factor for the $24\mu\text{m}$ data is given by Engelbracht et al. (2007) as $(4.54 \pm 0.18) \times 10^{-2}\text{ MJy sr}^{-1}$ [MIPS instrumental unit] $^{-1}$.

In the 70 and 160 μm data processing, the first step was to fit ramps to the reads to derive slopes. In this step, readout jumps and cosmic ray hits were also removed, and an electronic nonlinearity correction was applied. Next, the stim flash frames taken by the instrument were used as responsivity corrections. The dark current was subtracted from the data, and an illumination correction was applied. Short term variations in the the signal (often referred to as drift) were removed from the 70 μm data; this also subtracted the background from the data. Next, a robust statistical analysis was applied to cospatial pixels from different frames in which statistical outliers (e.g. pixels affected by cosmic rays) were masked out. Once this was done, final mosaics were made using square pixels of $4.5''$ for the 70 μm data and $9''$ for the 160 μm data. The backgrounds in the 160 μm data and the residual backgrounds in the 70 μm data were measured in regions outside the optical disks of the galaxies and subtracted, and then flux calibration factors were applied to the data. The 70 μm calibration factors given by Gordon et al. (2007) are $702 \pm 35 \text{ MJy sr}^{-1} [\text{MIPS instrumental unit}]^{-1}$ for coarse-scale imaging and $2894 \pm 294 \text{ MJy sr}^{-1} [\text{MIPS instrumental unit}]^{-1}$ for fine-scale imaging. The 160 μm calibration factor is given by Stansberry et al. (2007) as $41.7 \pm 5 \text{ MJy sr}^{-1} [\text{MIPS instrumental unit}]^{-1}$. An additional 70 μm nonlinearity correction given as

$$f_{70\mu\text{m}}(\text{true}) = 0.581(f_{70\mu\text{m}}(\text{measured}))^{1.13} \quad (1)$$

by Dale et al. (2007) was applied to coarse-scale imaging data where the surface brightness exceeded 66 MJy sr^{-1} .

4. Point Spread Functions and Image Fitting

For analyzing the radial profiles of the 70 and 160 μm data and for creating accurate models of the spatial distribution of 24 μm emission, we needed point spread functions (PSFs) that accurately represent the observed PSFs. While the STinyTim model (Krist 2002) can be used to model the PSF, the model output does not match the observed PSF of point sources. This is because the model assumes that the PSF is infinitesimally subsampled, whereas the observed PSF is measured with pixels that effectively blur some of the fine features. One approach to circumvent this problem is to simply smooth the model PSF (Gordon et al. 2007; Stansberry et al. 2007). As an alternative approach, we created a set of empirical PSFs from archival data.

The 24 and 70 μm PSFs were constructed using archival MIPS photometry mode data from program 20496 (PI: Marscher) of 3C 273, 3C 279, and BL Lac, which are relatively point-like infrared sources at these wavelengths. Data from a total of 25 AORs were used. These data were processed using the same techniques described in Section 3 except that the final mosaics were made for each AOR, and the images axes were left in the native instrumental rotation instead of being aligned with the J2000 coordinate system. The final PSFs were created by normalizing the flux densities of every mosaic to 1 and then median combining the frames from all AORs, which filtered out extended emission such as a tail-like feature extending north of 3C 273.

MIPS 160 μm photometry mode observations of compact sources typically do not completely

sample the PSF, so we needed to use scan map data to create a PSF at this wavelength. In this case, we used SINGS data of Mrk 33, NGC 1266, NGC 1377, NGC 3265, and NGC 3773 to create the PSF. These galaxies were selected because they are galaxies from SINGS that are unresolved or marginally resolved at $24\ \mu\text{m}$, so we can safely assume that the $160\ \mu\text{m}$ counterparts are also unresolved. These data were processed in the same way as the $160\ \mu\text{m}$ photometry data for the elliptical galaxies in this paper except that an additional drift removal step was applied to the data, separate final mosaics were made for each AOR, and the images axes were left in the native instrumental rotation. As with the 24 and $70\ \mu\text{m}$ PSFs, the final PSF was created by normalizing the flux densities of every mosaic to 1 and then median combining the frames from all AORs.

The $70\ \mu\text{m}$ and $160\ \mu\text{m}$ emission from our CO-rich targets is very poorly resolved, so no detailed morphological analysis was done in these bands. However, the $24\ \mu\text{m}$ emission is resolved, and simple model fits are made to parametrize the $24\ \mu\text{m}$ morphologies. We used the image fitting techniques described by Bendo et al. (2006) to characterize the spatial distribution of the $24\ \mu\text{m}$ dust emission and to measure the flux densities of the galaxies. These techniques have been improved in several ways compared to the models that Bendo et al. (2006) applied to the Sombrero Galaxy. First, we are now using the empirical PSFs described above instead of the STinyTim theoretical PSFs. With these PSFs, we can more accurately model the region near the centers of these galaxies. Second, we now treat the central coordinates of each model component as free parameters. The models used in this paper include unresolved point sources, inclined exponential disks, de Vaucouleurs ($R^{1/4}$) profiles, and rings with exponential profiles as well as combinations of these, all of which are convolved with the empirical $24\ \mu\text{m}$ PSF.

5. Ancillary Data

In addition to the CO observations cited above, we also compare the mid-IR morphology to that of the $1.4\ \text{GHz}$ radio continuum, the stellar distributions from optical and NIR images, and the dust seen in silhouette against the optical continuum. The $1.4\ \text{GHz}$ radio continuum emission from galaxies originates in both AGN activity and star formation (Condon 1992). Active nuclei should be distinguishable as nuclear point sources, perhaps with a jet, whereas kpc-scale extended emission more likely originates from star formation (Wrobel & Heeschen 1988).

Radio continuum images (and one nondetection) for UGC 1503, NGC 807, NGC 3656, NGC 4476, and NGC 5666 have been published by Lucero & Young (2007). The FIRST survey (Becker, White, & Helfand 1995) provides radio continuum images of NGC 2320, NGC 3032, NGC 4459, and NGC 4526. All of these $1.4\ \text{GHz}$ images have resolutions on the order of $5''$, which facilitates comparisons to the MIPS $24\ \mu\text{m}$ images at $6''$ resolution. Table 2 lists the beam sizes and rms noise levels of the continuum images. It also shows that while the FIRST images have typically a factor of 3 to 4 higher noise levels than our own, they do not have systematically lower signal-to-noise ratios. Thus we do not expect significant biases in the detectability of extended structures, for example, between the FIRST images and our own $1.4\ \text{GHz}$ data.

Broadband optical g and i images of NGC 3032, NGC 4459, and NGC 4526 were obtained from the Sloan Digitized Sky Survey (SDSS). V and R images of UGC 1503, NGC 807, NGC 2320, and NGC 3656 were obtained by L. van Zee in November 2002 with the Mini-Mosaic Imager (MiniMo) on the WIYN 3.5m telescope and were reduced as described by Young (2005). The seeing in those images ranged from $0.9''$ to $1.3''$. V and I images of NGC 4476 and NGC 5666 were obtained with the Kitt Peak 2.1m telescope and T2KA CCD in April 2003. Exposure times for those images were 1200 s in V and 1800 s in I ; the seeing varied from $1.1''$ to $1.6''$ in those images and they were reduced in the same manner as for the WIYN MiniMo images. Finally, WFPC2 images of NGC 3032, NGC 4459, and NGC 4526 in the F606W or F555W filters were retrieved from the HST archive along with ACS observations of NGC 4476.

The $24\mu\text{m}$ emission from NGC 807 is also compared with the distribution of HI in the galaxy. HI emission was mapped with the National Radio Astronomy Observatory’s Very Large Array¹ in its C configuration for 6 hours on 2002 Dec 10 and 6 hours on 2002 Dec 16 in program AY135. The total bandwidth was 3.125 MHz centered at 4650 km s^{-1} , giving 63 channels of 21.3 km s^{-1} . The absolute flux scale, bandpass calibration, and time dependent gain corrections were determined from observations of the nearby source J0137+331. All data calibration and image formation were done using standard calibration tasks in the AIPS package; continuum emission was subtracted directly from the visibility data by making first order fits to the line-free channels. The calibrated data were Fourier transformed using Briggs’ robust weighting scheme with a robustness parameter of 0.0, which gave a resolution of $13.8'' \times 13.1''$ and a rms noise level of $0.2 \text{ mJy beam}^{-1}$. The dirty images were cleaned down to a residual level approximately equal to the rms noise fluctuations. The integrated intensity image was made by smoothing, clipping, and then summing the cleaned data cube in a manner similar to that used by Young et al. (2008).

6. Results

6.1. Flux Densities and Spectral Energy Distributions

None of the CO-rich early-type galaxies are pure point sources at $24\mu\text{m}$. All are resolved, though they are significantly less extended than the stellar distributions in the NIR and optical. Total flux densities at $24\mu\text{m}$ are thus derived from large aperture photometry in the sky-subtracted images. Unrelated point sources were first cleaned from the vicinity of the target using the task *imedit* in IRAF, and the total flux densities were summed in a series of circular apertures up to 60 pixels ($90''$) in radius. The total flux densities converge to within $\sim 2\%$ for radii $\geq 75''$, and therefore Table 3 quotes the flux density within the $75''$ aperture. A color correction is derived based on the power law index β ($S \propto \nu^\beta$) between the $24\mu\text{m}$ and $70\mu\text{m}$ flux densities; the power law

¹The National Radio Astronomy Observatory is operated by Associated Universities, Inc., under cooperative agreement with the National Science Foundation.

indices range from -1.9 to -3.0 . These indices are consistent with the mid-IR spectra of nearby galaxies presented by Smith et al. (2007). The color corrections tabulated by Stansberry et al. (2007) are 0.960 to 0.967. The dominant uncertainty in the flux densities is that of the absolute calibration, roughly 4% (Engelbracht et al. 2007).

The $70\mu\text{m}$ and $160\mu\text{m}$ emission generally appear unresolved (Section 6.3), so we treated these as point sources when measuring flux densities at these wavelengths. To select aperture and color corrections for the 70 and 160 μm data, we first fit the 60-160 μm IRAS and *Spitzer* data with unmodified blackbody functions to roughly characterize the SEDs. The typical color temperatures derived from these fits were $\sim 30\text{-}50$ K.

We choose to measure flux densities in the 70 μm data within an aperture of $81''$ radius, as it is the maximum aperture that stays entirely within the field-of-view of our $70\mu\text{m}$ images. Gordon et al. (2007) do not specifically quote an aperture correction for these parameters, so we derived that correction factor. The STinyTim model (Krist 2002) was used to create $60'$ -wide model PSFs for blackbodies with temperatures of 30, 40, and 50 K. After estimating the “background” level in an annulus of radii $81''$ to $100''$, we measured the fraction of the total flux density in a circle of radius $81''$. This procedure gives an aperture correction of 1.14 ± 0.02 . We also verified that we were able to reproduce the aperture corrections quoted in Gordon et al. (2007) to within 1%. We take the color correction for a black body of temperature 40 ± 10 K as 0.886 ± 0.015 (Stansberry et al. 2007).

In most of our targets, the dominant contribution to the uncertainty in the $70\mu\text{m}$ flux density is that of the absolute calibration scale (10% for fine scale data and 5% for coarse scale data, Stansberry et al. 2007). However, the images of NGC 2320 and NGC 4476 still suffer from some negative artifacts just outside the first Airy ring. Initial exploration suggests that the $70\mu\text{m}$ flux densities of these galaxies may be 20% and 10% low, respectively.

Flux densities in the $160\mu\text{m}$ images were measured in an aperture of radius $64''$ with sky background determined in an annulus of radii $80''$ to $160''$. For this aperture and a PSF approximately represented by a 40 K blackbody, we take an aperture correction from Stansberry et al. (2007) as an interpolation between a 30 K and a 50 K blackbody, which gives 1.3575 ± 0.0035 . The color correction, assuming a blackbody of 40 ± 10 K, is 0.964 ± 0.010 (Stansberry et al. 2007). For NGC 4459 and NGC 4526, the small fields of view made it difficult to estimate the background level and flux densities for these two should be treated with greater caution. Aside from the background level and the nonlinearity effect discussed below, the dominant contribution to uncertainty in the $160\mu\text{m}$ flux densities is the absolute calibration scale (12%, Stansberry et al. 2007).

Additional uncertainties in the flux densities come from the fact that the targets are bright at $70\mu\text{m}$ and $160\mu\text{m}$. Gordon et al. (2007) have shown that aperture photometry gives systematically lower flux densities than a PSF fitting technique, for sources brighter than about 1 Jy at $70\mu\text{m}$. The effect is roughly 5% at 2 Jy. The nonlinearity correction of Dale et al. (2007) (Section 3) should mitigate this effect for the coarse scale data of NGC 4526 and NGC 4459, but the correspond-

ing correction is not known for fine-scale data and the effect could be important for NGC 3032, NGC 3656, and NGC 5666. Stansberry et al. (2007) also show that sources brighter than 2 Jy at $160\mu\text{m}$ are underestimated, with the effect being as large as 20% at 4 Jy. Finally, we note that since the $160\mu\text{m}$ emission for NGC 807 is slightly resolved its aperture correction may be low.

NGC 807 and NGC 5666 also have FIR flux density measurements from the ISO satellite (Temi et al. 2004). In the case of NGC 807, the $160\mu\text{m}$ flux density of 2.39 ± 0.29 Jy that we derive from the MIPS data is consistent with the 2.8 ± 0.8 Jy measured by Temi et al. at $150\mu\text{m}$. For NGC 5666, our MIPS $160\mu\text{m}$ flux density (2.48 ± 0.30 Jy) seems low in comparison with the ISO data (3.9 ± 1.2 Jy at $150\mu\text{m}$ and 2.7 ± 0.8 Jy at $200\mu\text{m}$), but given the sizes of the uncertainties we cannot conclude that those three values are inconsistent with each other. We note that the analysis and processing of the MIPS $160\mu\text{m}$ data is routine, whereas the ISO data for NGC 807 and NGC 5666 were obtained with the PHT 32 mode, which is known to suffer from strong transient effects that make it difficult to calibrate (Temi et al. 2004).

Far-IR spectral energy distributions for our targets are shown in Figure 1, where we have included the $60\mu\text{m}$ and $100\mu\text{m}$ IRAS flux densities and $350\mu\text{m}$ observations of Leeuw et al. (2008) (see Table 4). The SEDs are similar to those of the “typical” spiral galaxy from the SINGS survey (Dale et al. 2005, 2007), but with $70/160\mu\text{m}$ colors slightly warmer than that of a typical spiral and $24/70\mu\text{m}$ colors slightly cooler than the spiral. The IRAS $60\mu\text{m}$ and $100\mu\text{m}$ flux densities, MIPS $70\mu\text{m}$ and $160\mu\text{m}$ flux densities and (where available) $350\mu\text{m}$ flux densities have been fitted with a blackbody modified with an emissivity $\propto \lambda^{-2}$ to characterize the dust temperatures in these galaxies. These color temperatures are given in Table 3. We find that the modified blackbody temperatures of 25-28 K for most of these galaxies are a few degrees warmer than the average color temperatures for spiral galaxies found by Dunne & Eales (2001), Popescu et al. (2002), and Bendo et al. (2003), which range from ~ 18 K to ~ 25 K depending on the number of thermal components and combinations of wave bands used. However, the color temperatures of the early-type galaxies in this paper are similar to the color temperatures measured in early-type galaxies by Bendo et al. (2003) and Leeuw et al. (2008). In contrast, the color temperatures of 22-23 K measured for NGC 807 and NGC 2320 are closer to those of spiral galaxies than to other elliptical and SO galaxies.

If the dust opacities in the diffuse ISM of most early-type galaxies are low, the dust producing the FIR cirrus emission could be bathed in a somewhat more intense or harder radiation field than is typical for spirals. This scenario could explain the higher color temperatures measured in the $60\mu\text{m}$ – $350\mu\text{m}$ range. However, since $24\mu\text{m}$ emission primarily traces hot dust associated with star-forming regions in spiral galaxies, the $24\mu\text{m}$ emission in these early-type galaxies could be relatively faint compared to the cirrus emission if these galaxies contain relatively little star formation compared to their dust content.

6.2. 24 μ m Morphology

In all of the targets, the 24 μ m emission is resolved. A variety of structures (point sources, rings, disks, and $r^{1/4}$ profiles) are evident in the images and are discussed in greater detail below. The interpretation of these structures is complicated by the fact that the 24 μ m intensity is a function of both the dust surface density and the illuminating radiation field. Possible dust heating sources include the post-main sequence stellar population, star formation regions, and AGN. (None of our targets have strong enough radio jets for spatially resolved synchrotron emission to be important at 24 μ m.) Thus, the 24 μ m emission by itself may not necessarily indicate the presence of star formation. However, evidence from the CO and radio continuum helps to resolve some of these ambiguities. For example, star formation is expected to be accompanied by cm-wave radio continuum emission (Condon 1992), whereas dust heated by the radiation from evolved stars would not be. Therefore the comparisons with the distribution of the molecular gas (the raw material for star formation) and the radio continuum provide constraints on the origin of the 24 μ m emission.

For each galaxy we consider in detail the evidence for star formation activity, with a particular view to distinguishing how much of the 24 μ m emission is due to star formation. We take the molecular gas to be the raw material, so that star formation should only be found within the CO disks. We ask whether the radio continuum emission is resolved on scales similar to the molecular gas, which (if true) suggests that the radio continuum does not arise in AGN activity. We investigate whether the 24 μ m emission or its morphological sub-components are distributed like the radio continuum and molecular gas, which would strongly suggest star formation activity. A schematic summary is found in Table 5 with brief comments and additional evidence from the FIR/radio flux density ratios, optical emission lines, stellar populations or GALEX colors where those are available. The FIR/radio flux density ratios are discussed in greater detail in Section 7.2.

6.2.1. UGC 1503

Figure 2 presents optical, unsharp-masked, 24 μ m, CO, and radio images of UGC 1503. In addition, a smooth galaxy model was constructed using the Multi-Gaussian Expansion technique of Cappellari (2002) and the top left panel of the figure shows the ratio of the original V image to the MGE model. The unsharp-masked V image shows some fairly subtle mottling in the interior of the galaxy, with perhaps some hint of flocculent arm segments at radii less than about 10". This is the same region where we find a regularly rotating molecular gas disk (radius 15" = 5.2 kpc). The radio continuum emission is also found in an asymmetric ring of similar size. The 24 μ m image shows a central dip, which we have verified is not due to saturation, and this image is well fit with a ring of radius 4.8" \times 3.5" (1.6 \times 1.2 kpc). Table 6 gives the best-fit parameters describing the model of UGC 1503 and the other galaxies.

A dust distribution following the stellar photospheric emission would be centrally peaked, unlike the 24 μ m emission of UGC 1503. In addition, if an annulus of dust in UGC 1503 were

illuminated by an old stellar population it could conceivably reproduce the $24\mu\text{m}$ image, but as discussed above one would have to appeal to some other process for the origin of the radio continuum ring. For these reasons we argue that the simplest explanation for the CO, radio and FIR morphologies of UGC 1503 is that star formation is taking place in an annulus of the molecular/dust disk. The FIR/radio flux density ratios support this interpretation, as discussed further in Section 7.

While the global similarities between radio continuum and $24\mu\text{m}$ morphology indicate that star formation activity in a ~ 1.6 kpc ring powers them both, the details of their morphologies have implications for the propagation of the star formation through the galaxy. As Figure 2 suggests, the ridgeline of the radio continuum ring is clearly outside the ridgeline of the $24\mu\text{m}$ ring, so that the two most prominent radio peaks are $3''$ to $4''$ away from corresponding $24\mu\text{m}$ peaks. The effect is not caused by a difference in spatial resolution of the two bands; the radio continuum image has somewhat better resolution ($5'' \times 4.5'' \sim 1.7$ kpc) than the $24\mu\text{m}$ image ($6''$), and the absolute registration ought to be good to $1''$ or better. Neither is this the effect described in some detail by Murphy et al. (2008), in which the radio continuum emission looks like a smoothed version of the MIR or FIR image because the diffusion length of cosmic ray electrons is larger than the mean free path of the photons that heat the dust. Instead, as the radio continuum emission has a longer rise and decay timescale than FIR emission after a burst of star formation activity (Roussel et al. 2003), this offset could indicate that the star formation activity is propagating inward or that the star formation rate is decreasing more strongly in the outer parts of the ring than the inner parts.

6.2.2. NGC 807

Figure 3 shows the $24\mu\text{m}$ emission from NGC 807 along with an optical image, optical dust maps, CO line emission and 20 cm radio continuum emission. The dust distribution traced in the $V - R$ color map and in the MGE residuals suggests a symmetric, dynamically relaxed disk. The $24\mu\text{m}$ emission from NGC 807 shows an unresolved peak on the nucleus of the galaxy, an elongated plateau and a surrounding envelope. The structure of the emission is well fit by a superposition of a nuclear point source (3.4 mJy), an exponential disk of scale length $17'' = 5.4$ kpc, and a plateau or a flat-topped inner disk whose flat region has a semimajor axis $11'' = 3.5$ kpc. The two disks each contain roughly 50% of the total $24\mu\text{m}$ flux density and the point source only about 5% of the total. At surface brightness levels of 1.2 MJy sr^{-1} and higher (20% of the peak), the $24\mu\text{m}$ emission shows a high degree of reflection symmetry. That fact is significant because both the molecular gas and radio continuum emission are notably stronger in the southeast and their peaks are $6''$ southeast of the optical/ $24\mu\text{m}$ nucleus. (It is worth noting that the radio continuum emission from NGC 807 is quite faint and data of higher sensitivity would be beneficial.)

The nuclear point source component of the $24\mu\text{m}$ image might be related to either an AGN or to unresolved nuclear star formation. It is curious, though, that no corresponding nuclear peak is found in the radio continuum emission. The plateau or flat-topped disk component is too extended

to be attributed to an AGN, and as it does not follow the stellar distribution either, it is unlikely to be the type of circumstellar dust emission discussed by Temi et al. (2008). This component could conceivably originate in star formation in the molecular disk since its size scale is similar to that of the molecular gas. (The CO dist extends to radii $\approx 20''$, and the plateau is flat to a semimajor axis $11''$ and declines with a scale length of $4''$ beyond.) The third component in NGC 807, the exponential component with a scale length of $17''$, could also conceivably originate in star formation in the molecular gas or it could trace circumstellar emission.

If star formation activity strictly depends on the kpc-scale local gas surface density, as in a Kennicutt-Schmidt relation (Kennicutt et al. 2007), we would expect it to be asymmetrically distributed like the molecular gas. But in the region where the molecular gas is found (radii less than $20''$) the $24\mu\text{m}$ emission lacks this asymmetry, and this observation suggests that either the $24\mu\text{m}$ emission is not primarily dust heated by star formation or that the local star formation rate is determined by something else in addition to the local gas density. The radio continuum emission does seem consistent with star formation in the molecular gas in both morphology and in total flux density (Section 7). In linear size this is quite a large star-forming disk; the radius of the molecular disk is $20'' = 6$ kpc. Thus, it seems likely that the $24\mu\text{m}$ emission may arise partly from star formation activity, but it must also include a substantial contribution from more symmetrically distributed heat sources such as an evolved stellar population and a nuclear source.

A unique feature of the $24\mu\text{m}$ emission in NGC 807 is the very low level, smooth emission extending to the west and northwest sides of the galaxy at radii of $20''$ to $60''$ (6 to 19 kpc; Figures 3 and 4). This emission is at surface brightness levels of 0.1 MJy sr^{-1} to 0.3 MJy sr^{-1} (3σ to 10σ), and it is not accounted for in the parametric fit described above. Figure 4 shows that the $160\mu\text{m}$ emission is also extended to the northwest over the same spatial region. Similar asymmetries are found in the broadband optical and HI images and are undoubtedly caused by a gravitational interaction that has left large-scale disturbances in the outer parts of the galaxy. For example, in the northeast and southwest corners of the HI image in Figure 4 there are sections of tidal arms that stretch beyond the frame to radii of $5'$ (91 kpc). HI column densities northwest of the galaxy nucleus peak at $8.6 \times 10^{20} \text{ cm}^{-2}$ ($9.4 \text{ M}_{\odot} \text{ pc}^{-2}$, including helium) at a resolution of $14''$ (4.2 kpc); this HI column density occurs $50''$ from the nucleus of the galaxy, and is the brightest HI emission at radii $\geq 20''$ by a factor of two. Thus, the low level asymmetries in the $24\mu\text{m}$ and $160\mu\text{m}$ images of NGC 807 are probably consistent with an interstellar dust component that is distributed like the atomic gas.

6.2.3. NGC 2320

Young (2005) showed that the V morphology of NGC 2320 is well described by an $r^{1/4}$ profile out to a semimajor axis of at least $90''$, which bolsters its classification as an elliptical even though it has quite a large molecular gas mass of $4 \times 10^9 \text{ M}_{\odot}$. The $V - R$ image of Figure 5 clearly shows the inner dust disk to be $20''$ in diameter, with somewhat enhanced reddening $10''$ southeast of the

nucleus. The unsharp-masked image also shows a bright ring of $35''$ diameter. Molecular gas in NGC 2320 is distributed rather like the dust in the $V - R$ image and it also shows a “tail” of gas to the southeast of the nucleus. In contrast, the radio continuum emission is not well resolved, with $\text{FWHM} \lesssim 1.7''$ (Becker, White, & Helfand 1995), and it is believed to be powered by AGN activity as described in greater detail by Young (2005).

Unlike the CO distribution in NGC 2320, the $24\mu\text{m}$ emission is notably symmetric. It is well described by a $r^{1/4}$ model whose half-light ellipse has semimajor and semiminor axes $4'' \times 2''$ (1.6×0.8 kpc; Table 6). The $24\mu\text{m}$ $r^{1/4}$ model is much more compact than the optical emission from the galaxy, though. Measured values for the effective or half-light radius of this galaxy range from $13''$ (J , 2MASS Extended Source Catalog) to $29.5''$ (V , Cretton et al. 2000) to $37''$ ($\sim B$, de Vaucouleurs et al. 1991), but all are significantly larger than our fitted half-light radii at $24\mu\text{m}$. We have confirmed the discrepancy in effective radii by convolving the 2MASS J image with the $24\mu\text{m}$ PSF and additionally by running our model fitting software on the original 2MASS J image to recover the effective radius in the same way as was done for the $24\mu\text{m}$ image. We find an effective radius of $23.4'' \pm 0.07''$ at J , more than five times larger than the $24\mu\text{m}$ effective radius. In this respect NGC 2320 is different from the ellipticals studied by Temi et al. (2008), which had very similar effective radii at optical/NIR and $24\mu\text{m}$. The difference in scale sizes implies that the $24\mu\text{m}$ emission from NGC 2320 is not primarily circumstellar dust around evolved stars, unless there is a strong age gradient in the stellar population such that the inner arcseconds host a larger proportion of intermediate-age stars that are relatively bright at $24\mu\text{m}$.

It is possible that the $24\mu\text{m}$ emission in NGC 2320 is attributable to star formation activity that is restricted to the central portions of the molecular disk. The $24\mu\text{m}$ emission does not show the same “tail” to the southeast that is seen in the molecular gas, but these might still be self-consistent if the molecular “tail” is locally gravitationally stable (perhaps not yet settled into its equilibrium orbit) or if the local star formation rate has a dependence on gas surface density that is steeper than linear. The CO column densities $10''$ southeast of the nucleus are at least a factor of 3 lower than the peak in the center of the galaxy, and if the star formation rate (traced by $24\mu\text{m}$ emission) were proportional to the square of the local molecular surface density then the $24\mu\text{m}$ emission $10''$ southeast of the nucleus would be a factor of 10 fainter than the nuclear value. But since the pointlike radio continuum emission cannot be attributed to star formation activity the current data do not necessarily favor star formation as the heating source for the $24\mu\text{m}$ emission. More detailed analysis of the ionized gas and the stellar population itself would provide important circumstantial evidence about the origin of the $24\mu\text{m}$ emission in this case.

6.2.4. NGC 3032

CO observations of this lenticular galaxy have recently been published by Young et al. (2008), and Figure 6 shows the comparison between optical, mid-IR, CO and radio morphology. A clearly defined dusty disk of diameter $28''$ is viewed at rather low inclination. The molecular disk is

coincident with this dust disk, but it also has a tail stretching to the southeast, and the tail has no obvious dust counterpart. Since the molecular gas is nearly exactly counterrotating with respect to the stellar rotation (Young et al. 2008), it is most likely to have been accreted from another galaxy or from the intergalactic medium into its retrograde orbit, and the asymmetric tail may be the remnant of the settling process. Radio continuum emission from NGC 3032 is very marginally resolved but is elongated in the same direction as the dust and stellar disks. The $24\mu\text{m}$ emission from the galaxy is also very marginally resolved, being well fit by an exponential disk of scale length $1.8''$ (0.19 kpc; Table 6). We find a marginal detection of an off-nuclear point source that may or may not be physically related to NGC 3032.

Similarly to NGC 2320, and unlike the cases described in Temi et al. (2008), the $24\mu\text{m}$ emission is a poor match to the optical/NIR structure of the galaxy. The 2MASS J image of NGC 3032 was analyzed in the same way as we have done for the $24\mu\text{m}$ images, and it was found best described by a model with 15% of the total luminosity in a compact nuclear source (probably a bright star cluster) and 85% in a $r^{1/4}$ spheroid with an effective semimajor axis of $87'' \pm 2''$. Thus, again, the $24\mu\text{m}$ emission is not primarily circumstellar dust heated by evolved stars.

The east-west elongations of the dust disk, the radio continuum emission and the bright part of the CO emission suggest that indeed star formation activity could be powering the radio and $24\mu\text{m}$ emission from NGC 3032. Radio and FIR flux densities are also consistent with star formation (Section 7), and there is other evidence for star formation activity in the optical line ratios (Sarzi et al. 2005) and stellar Balmer line absorption (Kuntschner et al. 2006). Interestingly, the young counterrotating stellar core found by McDermid et al. (2006a,b) has a radius of roughly $2''$, similar to the scale radius of the $24\mu\text{m}$ emission, and this young stellar core is rotating in the same direction as the molecular gas. Thus the optical data are entirely consistent with our interpretation that radio and $24\mu\text{m}$ emission in NGC 3032 arise in star formation. This star formation activity is most vigorous in the inner part of the molecular disk, which could be due to a nonlinear dependence of the star formation rate on the local gas density or to the gas disk being gravitationally stable in its outer regions.

6.2.5. NGC 3656

NGC 3656 is the most disturbed galaxy of this sample, being a clear example of a fairly recent merger remnant with a dramatic blue ring and shells. Figure 7 shows that the molecular gas is located in a nearly edge-on disk of radius $\approx 10'' = 1.9$ kpc, also clearly visible as a dark dust lane bisecting the nucleus. The structure of the dust lane is somewhat irregular, suggesting a warped or folded lane rather than the very thin, flat, relaxed disks seen in NGC 4526 and NGC 4459 (Sections 6.2.6 and 6.2.8). The radio continuum emission is clearly elongated in the same direction as the gas/dust disk, with a deconvolved Gaussian source size (HWHM) of $3.0'' \times 1.4''$ (Lucero & Young 2007). The $24\mu\text{m}$ emission is only modestly resolved but is also clearly elongated north-south, and is adequately fit by an exponential disk of scale length $2'' \pm 0.4'' = 0.39 \pm 0.08$ kpc and axis

ratio 0.3:1.0 (Table 6). Thus, the morphologies of radio continuum, 24 μm , and CO emission are all consistent with the interpretation that star formation powers the bulk of the radio and 24 μm emission. The scale sizes of the radio and 24 μm disks are substantially smaller than the molecular disk, as is also the case for NGC 3032. This result suggests that the local star formation rate or efficiency is higher in the inner part of the gas disk.

6.2.6. NGC 4459

The Virgo Cluster lenticular NGC 4459 clearly shows a relaxed, thin dust disk of semimajor axis $9'' = 0.7$ kpc (Figure 8), and the unsharp-masked HST image resolves the dust into a broad, flocculent outer annulus plus an inner ring of semimajor axis $2''$. The molecular gas lies in this regularly rotating disk, as shown in the channel maps presented by Young et al. (2008). The radio continuum emission from NGC 4459 is weak and unresolved— in fact, it is unusually weak, and is discussed further in Section 7. The 24 μm emission is very symmetric and also centrally concentrated but clearly resolved; it is well described by the sum of two exponential disks of scale radii $2.1''$ (0.16 kpc) and $33''$ (2.6 kpc). The more compact disk has 78% of the total 24 μm flux density.

The more extended ($33''$) 24 μm component in NGC 4459 is unlikely to be driven by star formation activity because its scale length is so much larger than the size of the molecular gas and dust disk. It may in fact trace circumstellar dust in an evolved stellar population as discussed by Temi et al. (2008). It is suggestive, though, that the size of the more compact 24 μm component, $2''$, is a good match to the size of the inner dust ring in the top right panel of Figure 8. The radio continuum source is also of a similar size. Thus it is possible that the compact 24 μm component and the radio continuum trace star formation activity in the central part of the gas disk (though we cannot rule out AGN activity on morphological grounds alone). Optical spectroscopy provides abundant evidence for active star formation in NGC 4459; the SAURON data show that the molecular disk coincides with an ionized gas disk of low $[\text{O III}]/\text{H}\beta$ ratio (Sarzi et al. 2005), strong Balmer absorption (Kuntschner et al. 2006), and a dynamically cold stellar subpopulation (Emsellem et al. 2004). If, then, 80% of the 24 μm and all of the radio continuum in NGC 4459 trace star formation activity, this is another case in which the efficiency must be much higher in the inner part of the gas disk than in the outer part.

6.2.7. NGC 4476

NGC 4476 is the second of our three Virgo Cluster early-type galaxies with well-developed dust disks (Figure 9). The F475W image also shows numerous bright point sources embedded in the dust. As for NGC 4459 and NGC 4526, the molecular gas is confined to this disk, which has a semimajor axis of $11'' = 0.9$ kpc. The bulk of the 24 μm emission can also be attributed to this dusty disk, as an excellent model of the image is achieved from a ring with its maximum

intensity at a semimajor axis of $6''$ (0.5 kpc) and gradually decreasing intensities on the interior and exterior (Table 6). Thus, there is extremely good agreement between $24\mu\text{m}$ morphology and CO morphology.

No radio continuum emission is detected from NGC 4476, and Lucero & Young (2007) hypothesize that the magnetic field and/or the relativistic electrons may have been stripped by interactions with the intracluster medium. Circumstantial evidence for this idea comes from the fact that no atomic gas is detected either (Lucero et al. 2005). We cannot, therefore, use the radio continuum morphology to argue that the $24\mu\text{m}$ emission indicates star formation activity in this case. However, GALEX images of NGC 4476 show significantly bluer colors at radii $\lesssim 12''$, becoming as blue as (FUV-NUV) ~ 1.2 mag in the central resolution element compared to (FUV-NUV) ~ 2.5 mag in the outskirts of the galaxy (Gil de Paz et al. 2007). In the absence of the radio continuum detection it is not obvious that the $24\mu\text{m}$ emission indicates star formation activity, but the optical point sources and the GALEX colors strongly suggest this interpretation.

6.2.8. NGC 4526

NGC 4526 is the third of our Virgo Cluster early-type galaxies with well-developed molecular and dust disks (Figure 10). The gas/dust disk is seen at high inclination and has a sharp outer edge at a semimajor axis of $15'' = 1.2$ kpc. The radio continuum morphology closely matches that of the molecular gas; the $24\mu\text{m}$ emission is described by a plateau or a flat-topped disk of semimajor axis $7.5''$ (0.6 kpc) and a more extended, rounder exponential disk of scale length $28''$ (2.4 kpc). The plateau contains 82% of the total flux density; given its size scale and orientation it is highly likely that this $24\mu\text{m}$ component is associated with the radio continuum emission via star formation in the molecular gas. The more extended, fainter and rounder $24\mu\text{m}$ component could well be attributed to circumstellar dust as in Temi et al. (2007), but it only contributes 18% of the $24\mu\text{m}$ flux density. Again, similar to the case of NGC 4459, the optical spectroscopy traces star formation activity and its after-effects in an ionized gas disk (Sarzi et al. 2005) and a young, dynamically cold stellar disk (Kuntschner et al. 2006; Emsellem et al. 2004) that have similar sizes to the molecular disk.

6.2.9. NGC 5666

NGC 5666 was originally classified as an elliptical, but upon closer inspection, its morphological status is uncertain. Color images (e.g. Figure 11) clearly show the red nucleus and a blue ring of radius approximately $5''$, which are also shown by Donzelli & Davoust (2003) (DD03). The ratio of the V image to its best-fit MGE model also shows one spiral arm at radii of $15'' - 20''$, and DD03 find blue star-forming knots in the arm. The arm would tend to suggest a spiral classification but it is not obvious that the bulge + exponential disk surface brightness fit of DD03 is well constrained or

is a better fit to the optical surface brightness profile than a $r^{1/4}$ law. In addition, DD03 comment that their bulge + disk decomposition has an unusually extended bulge and compact disk, with the effective radius of the bulge being larger than the scale length of the disk. The galaxy therefore does not seem a particularly close match to either a prototypical elliptical or a prototypical spiral. Measurements of the stellar velocity dispersion and rotation velocity (V_{max}/σ) would give better physical insight into the structure of this galaxy.

The molecular gas in NGC 5666 (Figure 11) is found in an inclined disk of radius roughly 7–8". Radio continuum emission is distributed in an asymmetric ring, brightest in the southeast and the northwest, with a central dip. Local maxima in the radio continuum emission are at radii of 3.5". The best fit model to the 24 μ m image is a flat-topped disk or plateau of radius 5.9" = 0.9 kpc, but the outer scale length is so small that the model is essentially an inclined top hat. The observed 24 μ m peak is offset a few arcseconds to the southeast of the galaxy nucleus and it coincides with the peak of the radio continuum emission.

In this case the very close matches between the size of the 24 μ m plateau, the extent of the molecular disk and the radio continuum ring (as well as the blue ring in optical images) strongly suggest that both the radio and 24 μ m emission are driven by star formation activity. Models in which the 24 μ m emission comes from a point source or is distributed like the stars are strongly ruled out.

6.3. 70 μ m and 160 μ m Images

The non-rotated images at 70 μ m and 160 μ m were fit with the isophotal analysis program *ellipse* in STSDAS, and the resulting surface brightness profiles are shown in Figures 12 and 13. From these comparisons it is evident that, with the exception of NGC 807, the targets are not resolved at 70 μ m and 160 μ m. NGC 807 is modestly resolved at 160 μ m and shows an elongation in the same sense as the 24 μ m image, as discussed already in Section 6.2.2.

7. Discussion

7.1. Corroboration of Star Formation: Mid-IR vs Near-IR

The 24 μ m morphologies in these CO-rich early-type galaxies show a variety of structures including disks, rings, point sources, and very faint smooth emission. We have argued that, at least in the cases of UGC 1503, NGC 3032, NGC 3656, NGC 4526, and NGC 5666, and possibly also in NGC 4476, the bulk of the 24 μ m emission must arise from dust heated by star-forming regions. In NGC 4526, we attribute the 24 μ m emission from the elongated, flat-top disk component (82% of the total flux density) to star formation and the rest to circumstellar emission. In NGC 4459, we have argued that 78% of the 24 μ m emission is in a modestly-resolved component that is probably

heated by star formation though it could conceivably also be powered by an active nucleus; the remaining 22% we attribute to circumstellar dust. In NGC 807, approximately half to 95% of the $24\mu\text{m}$ emission may be related to star formation activity. In NGC 2320 the origin of the $24\mu\text{m}$ emission is not clear, so the most that can be said is that studies of the stellar populations and the ionized gas distribution and line ratios would provide useful clues.

Our morphological work also indicated that in our CO-rich early type galaxies the $24\mu\text{m}$ emission usually traces the molecular gas and the silhouette dust disks more closely than it does the stellar distribution. In some cases this is fairly obvious, as the $24\mu\text{m}$ emission is best modeled by a ring or a structure that is flat at radii $6''$ to $11''$. In other cases the $24\mu\text{m}$ model is centrally peaked, but it has a radial scale length many times smaller than that of the stellar distribution as we have verified by analyzing near-IR J images in the same way as the $24\mu\text{m}$ images.

This result is an obvious contrast to the findings of Temi et al. (2007, 2008) that the $24\mu\text{m}$ emission in their elliptical galaxies closely traced the optical/NIR star light, with very similar size scales and fairly tight correlations between L_{24} and L_B . However, that circumstellar dust should also be present in all of our targets. It must simply be outshone by the star formation. As a test of this hypothesis, Figure 14 compares the $24\mu\text{m}$ flux densities and K_s apparent magnitudes of our sample galaxies to those of Temi et al. (2008). Integrated K_s total magnitudes are taken from the Two Micron All Sky Survey and its extended objects final release as tabulated in the NASA Extragalactic Database. The median $24\mu\text{m} / 2.2\mu\text{m}$ flux density ratio in the CO-rich early-type galaxies is a factor of 15 higher than that in the sample of Temi et al. (2008); in other words, the $24\mu\text{m}$ flux densities are 15 times larger than would be expected if the $24\mu\text{m}$ emission were entirely circumstellar in origin. In Figure 14 we also show the flux densities of the extended $24\mu\text{m}$ components of NGC 4459 and NGC 4526. On the basis of morphology we had previously argued that those components would be consistent with the circumstellar emission; here we show that their flux densities also support this interpretation because they fall on the $24\mu\text{m} - K_s$ correlation defined by the CO-poor ellipticals.

7.2. Additional Corroboration: FIR/Radio Ratios

Radio to FIR flux density ratios confirm the suggestions of star formation activity in all cases except NGC 2320. For the computation of these ratios we follow Yun, Reddy, & Condon (2001) (YRC), who have used IRAS $60\mu\text{m}$ and $100\mu\text{m}$ flux densities; the choice is made because YRC provide the most complete comparison set of FIR and radio continuum flux densities for many types of galaxies. The logarithmic FIR/radio ratio q is presented in Figure 15 for our sample of CO-rich early type galaxies as well as for YRC’s sample (which includes all galaxies having $100\mu\text{m}$ flux densities greater than 2 Jy) and the early-type galaxies of Temi et al. (2007).

According to the definitions of YRC, NGC 2320 is a radio excess galaxy whose radio continuum is likely powered by an AGN; this classification is consistent with its point source radio morphology.

NGC 4476 and NGC 4459 are FIR-excess galaxies. The remainder of the galaxies have FIR/radio ratios q that are consistent with those of star forming galaxies and that confirm our inferences based on the $24\mu\text{m}$ morphology. For comparison, the majority of the elliptical galaxies studied by Temi et al. (2007) are radio excess galaxies hosting AGN emission, though some of them do also sit near the star formation FIR-radio correlation.

The FIR-excess galaxies are rare, comprising 9 of 1809 galaxies in the sample of YRC, although they are somewhat more common in other samples of spirals (Roussel et al. 2003). Being rare, they are valuable for the insights they give into the physical processes underlying the FIR/radio correlation. For example, both YRC and Roussel et al. (2003) note that some of the FIR-excess galaxies have unusually high dust temperatures as indicated by IRAS $60\mu\text{m}/100\mu\text{m}$ flux density ratios ≥ 0.78 . Others have “normal” dust temperatures. YRC have argued that the “hot dust” FIR excess galaxies may be very densely enshrouded AGN or compact nuclear starbursts. Roussel et al. (2003, 2006) have argued that a few of the hot dust FIR excess galaxies are likely to be cases of recently initiated starbursts, in which the starburst began so recently that there has not yet been time for appreciable numbers of supernovae to accelerate the cosmic ray population and produce the cm-wave synchrotron emission. They have also argued that “cool dust” FIR-excess galaxies are dominated by heating from the evolved stellar population, not star formation (c.f. Temi et al. 2008).

All of the CO-rich targets studied here fall into the “cool dust” category, and our FIR excess galaxies NGC 4476 and NGC 4459 have IRAS $60/100\mu\text{m}$ flux density ratios of 0.36 and 0.39 respectively. Thus, of the three preceding explanations for the FIR excess phenomenon, we reject the idea of highly enshrouded AGN in our targets. We have also used morphology to argue that the bulk of the $24\mu\text{m}$ emission does not originate from dust heated by the evolved stellar population in NGC 4459. It is possible that recently initiated star formation could be responsible for the relatively low level of radio continuum emission in NGC 4476 and NGC 4459 (and perhaps also in NGC 0807 and NGC 4526, which have relatively high q values). Close inspection of their stellar populations could test that idea. An alternative, possibly viable explanation is that the weak radio continuum flux densities may be related to unusually weak magnetic fields. In the case of the Virgo cluster members NGC 4459, NGC 4476, and NGC 4526, the interactions with the intracluster medium could be responsible for stripping the plasma and/or the magnetic fields in a more advanced version of the stripping that is now evident in the Virgo spirals studied by Murphy et al. (2008). High quality radio polarization imaging would help to answer this question, and such work would also be valuable because rather little is known about the strengths of interstellar magnetic fields in early-type galaxies.

Draine et al. (2007) have made careful models of the mid- to far-IR emission in nearby spirals and have concluded that the FIR emission (specifically, emission at wavelengths longer than $100\mu\text{m}$) originates in the diffuse ISM, not star forming regions. If this is true, then the FIR emission in spirals may be a better tracer of the total dust mass than of the total light emitted from star-forming regions. FIR emission in spirals may still be associated with star formation, but as a cause rather

than an effect; the association could be through the Schmidt law in the same way that molecular clouds are associated with star formation. In this case, the tightness of the radio-FIR correlation is still puzzling. Galaxies that are rich in cold neutral gas but are not forming stars (such as NGC 2320?) should be particularly valuable test cases for disentangling the physical processes driving these emissions, and it would be helpful to have FIR images at spatial resolutions matching those of the molecular gas maps. Aside from the slight extension in the $160\mu\text{m}$ image of NGC 807 there is still very little information on the resolved FIR emission of early-type galaxies. One notable exception is that the ground-based observations of Leeuw et al. (2008) have clearly resolved the $350\mu\text{m}$ emission in at least UGC 1503, NGC 807, NGC 3656, and NGC 4476, and they show it to be elongated at the same orientation as our $24\mu\text{m}$ and CO images.

7.3. The Future and the History of these Galaxies

Calzetti et al (2007) find an empirical relation between the $24\mu\text{m}$ luminosity of a star-forming region or galaxy and its star formation rate:

$$\text{SFR} (M_{\odot} \text{ yr}^{-1}) = 1.27 \times 10^{-38} (L(24\mu\text{m}))^{0.885}.$$

Here $L(24\mu\text{m})$ is the monochromatic luminosity at $24\mu\text{m}$ in units of erg s^{-1} , given by $4\pi D^2 \nu S_{\nu}$ with S_{ν} being the flux density at $24\mu\text{m}$ and ν the central frequency of the $24\mu\text{m}$ band. If this relation is accurate in early-type galaxies as well (e.g. if the initial mass function is the same in both types of galaxies, among other issues), the star formation rates in our CO-rich targets are on the order of a few tenths of a solar mass per year (Table 7). Gas depletion timescales can be estimated from the total molecular gas mass (molecular hydrogen with a correction for helium) divided by the star formation rate. Those timescales are a few Gyr, with one exception. The $24\mu\text{m}$ luminosity of NGC 2320 is so low compared to its total molecular mass that even if all of its $24\mu\text{m}$ luminosity were powered by star formation the gas depletion timescale would be longer than the Hubble time.

Since the molecular gas in the early-type galaxies settles into kpc-scale disks (Young 2002, 2005; Young et al. 2008), the young stars will also be dynamically cold populations. The CO-rich early-type galaxies, with the exceptions already discussed, are building disk stellar components on timescales of a few Gyr. Indeed, in NGC 4526 the dynamically cold stellar disk is already visible in the stellar kinematics (Emsellem et al. 2004). However, since the total molecular gas masses are only a few $10^8 M_{\odot}$ to a few $10^9 M_{\odot}$, the young stellar populations will not make up more than a few percent of the total stellar mass.

The gas depletion timescales in Table 7 are similar to the corresponding timescales in the disks of spiral galaxies. Depletion timescales are, of course, very sensitive to assumptions about initial mass functions and CO-to- H_2 conversion factors, but estimates for spirals tend to be in the range of a few Gyr (Kennicutt 1998) and the values in Table 7 are 1 to 4 Gyr in seven of nine cases. In

other words, while the elliptical and lenticular galaxies have smaller molecular masses than spirals, their star formation efficiencies are similar to within factors of a few.

Kennicutt (1998) has also pointed out that recycled matter from stellar evolution (especially from the more massive stars) may make the gas reservoir last a factor of 2 to 3 times longer than the simple depletion timescale estimate. Thus, we can expect the molecular disks in the early-type galaxies to remain for many Gyr, perhaps as long as another Hubble time, unless there are significant destructive processes such as stripping, interactions with hot gas, and/or possible AGN feedback. Ram pressure stripping will be more intense in clusters than in the field, and tidal interactions more frequent, so the environments of our CO-rich early-type galaxies are also of interest. NGC 4476, NGC 4459, and NGC 4526 are members of the Virgo Cluster and NGC 2320 is a member of the Abell 569 cluster; NGC 4476 is already known to have suffered some ram pressure stripping (Lucero et al. 2005), but it still retains its molecular gas at least for the time being.

To put this disk growth into the broader context of galaxy formation and evolution, it is important to know what (if anything) the molecular content of an early-type galaxy reveals about its history. However, the origins of the molecular gas in early-type galaxies are not yet known in most cases, and it is not yet clear why some early-type galaxies are rich in molecular gas while others are not. For many years there has been speculation that the molecular gas could originate from the mass loss of evolved stars (e.g. Sage & Welch 2006, and references therein). In other cases such as NGC 3032 (Young et al. 2008) and NGC 2768 (Crocker et al. 2008), the clear kinematic misalignments between molecular gas and stars indicate that the molecular gas was accreted from some external source or possibly it is leftover from a major merger. It will be necessary to obtain larger numbers of molecular gas maps and better statistics on the CO content of the early-type galaxies before we will understand what fraction of their molecular gas could have come from internal and external origins, or whether the CO-rich and the CO-poor galaxies have had systematically different formation histories.

8. Summary

For the majority of the CO-rich early-type galaxies, the close agreements between CO, $24\mu\text{m}$, and radio continuum morphologies suggest that the bulk of the $24\mu\text{m}$ emission should be attributed to star formation activity. In our sample, these galaxies include UGC 1503, NGC 3032, NGC 3656, NGC 4459, NGC 4526, and NGC 5666. The $24\mu\text{m}$ emission in NGC 4476 is likely due to star formation. A portion of the $24\mu\text{m}$ emission from NGC 807 may also trace star formation activity, but the origin of the $24\mu\text{m}$ emission in NGC 2320 is not yet clear. Radio and FIR flux density ratios are consistent with this interpretation, as are the increased $24\mu\text{m}/K_s$ flux density ratios of the CO-rich over the CO-poor early-type galaxies. Thus, one of the major implications of this work is that the CO, radio, and MIPS data are roughly consistent with the UV results implying star formation activity in a few tens of percent of the nearby early-type galaxies. The necessary raw material is present, more or less, and the molecular gas is often being processed into stars.

In the cases of NGC 3032, NGC 3656, and NGC 4459, the star formation activity seems to be taking place on more compact spatial scales than the distribution of the gas itself. This situation could arise if the star formation rate is a strong (nonlinear) function of the local gas surface density, or if the molecular disks are only unstable to star formation in their inner portions.

However, the origin of the $24\mu\text{m}$ emission in the CO-rich early-type galaxies is not entirely clear-cut. An extended component in NGC 807 (detected both at $24\mu\text{m}$ and at $160\mu\text{m}$) may trace dust in the diffuse atomic ISM. Extended $24\mu\text{m}$ components in NGC 4459 and NGC 4526 may arise from dust around the evolved stars, just as Temi et al. (2008) find in the CO-poor early-type galaxies. Likewise, though NGC 2320 is very CO-rich, the mismatches between CO, radio continuum and $24\mu\text{m}$ morphology make it unclear how much (if any) star formation is occurring there. In these cases, detailed comparisons with the UV morphologies and the stellar populations would provide firmer information about the distribution of star formation activity (or the lack of it) within the galaxies' molecular disks.

This work also opens the way for more quantitative tests of theoretical and phenomenological models of the star formation process. For example, with a model of the gravitational potential (from the stellar distribution and a mass-to-light ratio), it would be possible to test whether the Toomre-type local gravitational instability is consistent with the locations of star formation activity, as discussed by Kawata et al. (2007). The gas-rich early-type galaxies could also provide useful perspective on the workings of the Kennicutt-Schmidt relationship between the star formation rate and the gas surface density. If these models have truly captured some underlying physics of the star formation process they ought to work in the ellipticals and lenticulars as well as in the spirals.

LMY thanks the University of Oxford sub-department of Astrophysics and the Imperial College department of Astrophysics for their hospitality. Scott Montgomery provided assistance in the early stages of the project. We also thank Liese van Zee for the WIYN images and Daniel A. Dale for the use of his SED template and for discussions about his results. This research has made extensive use of the NASA/IPAC Extragalactic Database (NED) which is operated by the Jet Propulsion Laboratory, California Institute of Technology, under contract with the National Aeronautics and Space Administration. This work is based on observations made with the *Spitzer Space Telescope*, which is operated by the Jet Propulsion Laboratory (JPL), California Institute of Technology under NASA contract 1407. Support for this work was provided by NASA and through JPL Contract 1277572.

REFERENCES

- Becker, R. H., White, R. L., & Helfand, D. J. 1995, ApJ, 450, 559
Bendo, G. J., Joseph, R. D., Wells, M., et al. 2002, AJ, 123, 3067
Bendo, G. J., Joseph, R. D., Wells, M., et al. 2002, AJ, 124, 1380

- Bendo, G. J., Joseph, R. D., Wells, M., et al. 2003, *AJ*, 125, 2361
- Bendo, G. J., Calzetti, D., et al. 2007, *MNRAS*, 380, 1313
- Bendo, G. J., Buckalew, B. A., Dale, D. A., et al. 2006, *ApJ*, 645, 134
- Calzetti, D., Kennicutt, R. C., Engelbracht, C. W., et al. 2007, *ApJ*, 666, 870
- Cappellari, M., 2002, *MNRAS*, 333, 400
- Combes, F., Young, L. M., & Bureau, M. 2007, *MNRAS*, 377, 1795
- Condon, J. J. 1992 *ARAA* 30, 575
- Condon, J. J., Cotton, W. D., Greisen, E. W., Yin, Q. F., Perley, R. A., Taylor, G. B., & Broderick, J. J. 1998, *AJ*, 115, 1693
- Cretton, N., Rix, H.-W., & de Zeeuw, P. T. 2000, *ApJ*, 536, 319
- Crocker, A. F., Bureau, M., Young, L. M., & Combes, F. 2008, *MNRAS*, 386, 1811
- Dale, D. A., et al., 2007, *ApJ*, 655, 863
- Dale, D. A., Bendo, G. J., Engelbracht, C. W., et al. 2005, *ApJ*, 633, 857
- de Zeeuw, P. T., et al. 2002, *MNRAS*, 329, 513
- de Vaucouleurs, G., de Vaucouleurs, A., Corwin Jr., H.G., Buta, R. J., Paturel, G., & Fouque, P. 1991, *Third Reference Catalogue of Bright Galaxies, Version 3.9* (Berlin: Springer-Verlag)
- Donzelli, C. J., & Davoust, E. 2003, *A&A*, 40, 91
- Draine, B. T., Dale, D. A., Bendo, G. J., et al. 2007, *ApJ*, 663, 866
- Dunne, L., & Eales, S. A. 2001, *MNRAS*, 327, 697
- Engelbracht, C. W., et al. 2007, *PASP*, 119, 994
- Emsellem, E., et al. 2004, *MNRAS*, 352, 721
- Fukugita, M., Nakamura, O., Turner, E. L., et al. 2004, *ApJ*, 601, L127
- Gil de Paz, A., Boissier, S., Madore, B. F., et al. 2007, *ApJS*, 173, 185
- Goudfrooij, P., Hansen, L., Jorgensen, H. E., & Norgaard-Nielsen, H. U. 1994, *A&AS*, 105, 341
- Gordon, K. D., et al., 2005, *PASP*, 117, 50
- Gordon, K. D., et al., 2007, *PASP*, 119, 1019

- Jensen, J. B., Tonry, J. L., Barris, B. J., Thompson, R. I., Liu, M. C., Rieke, M. J., Ajhar, E. A., & Blakeslee, J. P., 2003, *ApJ*, 583, 712
- Kaneda, H., Onaka, T., Kitayama, T., Okada, Y., & Sakon, I. 2007, *PASJ*, 59, 107
- Kaviraj, S., Schawinski, D., Devriendt, J. E. G., et al. 2007, *ApJS*, 173, 619
- Kawata, D., Cen, R., & Ho, L. C. 2007, *ApJ*, 669, 232
- Kennicutt, R. C. Jr. 1989, *ApJ*, 344, 685
- Kennicutt, R. C. Jr. 1998, *ARA&A*, 36, 189
- Kennicutt, R. C., Jr., et al. 2003, *PASP*, 115, 928
- Kennicutt, R. C. Jr., Calzetti, D., Walter, F., et al. 2007, *ApJ*, 671, 333
- Knapp, G. R., Private Communication, quoted in the NASA Extragalactic Database
- Knapp, G. R. & Rupen, M. P. 1996, *ApJ*, 460, 271
- Krist, J. 2002, *Tiny Tim/SIRTF User’s Guide* (Pasadena: SSC)
- Kuntschner, H., Emsellem, E., Bacon, R., Bureau, M., et al. 2006, *MNRAS*, in press (astro-ph/0602192)
- Lees, J. F., Knapp, G. R., Rupen, M. P., & Phillips, T. G. 1991, *ApJ*, 379, 177
- Leeuw, L. L., Davidson, J., Dowell, C. D., & Matthews, H. E. 2008, *ApJ*, 677, 249
- Lucero, D. M., & Young, L. M. 2007, *AJ*, 134, 2148
- Lucero, D. M., Young, L. M., & van Gorkom, J. H. 2005, *AJ*, 129, 647
- Macchetto, F., Pastoriza, M., Caon, N., et al. 1996, *A&AS*, 120, 463
- McDermid, R. M., Emsellem, E., Shapiro, K. L., et al. 2006, *MNRAS*, 373, 906
- McDermid, R. M., Bacon, R., Kuntschner, H., et al. (2006), *NewAR*, 49, 521
- Mei, S., et al., 2007, *ApJ*, 655, 144
- Morganti, R., de Zeeuw, P. T., Osterloo, T. A., McDermid, R. M., Krajnović, D., Cappellari, M., Kenn, F., Weijmans, A., & Sarzi, M. 2006, *MNRAS*, 371, 157
- Murphy, E. J., Helou, G., Kenney, J. D. P., Armus, L., & Braun, R. 2008, *ApJ*, 678, 828
- Murphy, E. J., Kenney, J. D. P., Helou, G., et al. 2008, in “The Evolving ISM in the Milky Way and Nearby Galaxies,” proceedings of the third Spitzer conference, Pasadena, 2007 (astro-ph:0802.2281)

- Okuda, T., Kohno, K., Iguchi, S., & Nakanishi, K. 2005, *ApJ*, 620, 673
- Popescu, C. C., Tuffs, R. J., Völk, H. J., Pierini, & Madore, B. F. 2002, *ApJ*, 567, 221
- Prieto, J. L., Rest, A., & Suntzeff, N. B., 2006, *ApJ*, 647, 501
- Reindl, B., Tammann, G. A., Sandage, A., & Saha, A., 2005, *ApJ*, 624, 532
- Riess, A. G., et al., 2004, *ApJ*, 607, 665
- Rogers, B., Ferreras, I., Lahav, O., et al. 2007, *MNRAS*, 382, 750
- Roussel, H., Helou, G., Beck, R., et al. 2003, *ApJ*, 593, 733
- Roussel, H., Helou, G., Smith, J. D., et al. 2006, *ApJ*, 646, 841
- Sage, L. J., & Welch, G. A. 2006, *ApJ*, 644, 850
- Sage, L. J., Welch, G. A., & Young, L. M. 2007, *ApJ*, 657, 232
- Sarzi, M., Falcón-Barroso, J., Davies, R. L., Bacon, R., Bureau, M., et al. 2005, *MNRAS*, 366, 1151
- Schawinski, K., Kaviraj, S., Khochfar, S., et al. 2007a, *ApJS*, 173, 512
- Schawinski, K., Thomas, D., Sarzi, M., et al. 2007b, *MNRAS*, 382, 1415
- Shields, J. C. 1991, *AJ* 102, 1314
- Smith, J. D. T., Draine, B. T., Dale, D. A., et al. 2007, *ApJ*, 656, 770
- Stansberry, J. A., et al., 2007, *PASP*, 119, 1038
- Temi, P., Brighenti, F., & Mathews, W. G. 2008, *ApJ* 672, 244
- Temi, P., Brighenti, F., & Mathews, W. G. 2007, *ApJ* 660, 1215
- Temi, P., Brighenti, F., Mathews, W. G., & Bregman, J. D. 2004, *ApJS*, 151, 237
- Tonry, J. L., Dressler, A., Blakeslee, J. P., et al. 2001, *ApJ*, 546, 681
- Wang, X., Wang, L., Pain, R., Zhou, X., & Li, Z., 2006, *ApJ*, 645, 488
- Welch, G. A., & Sage, L. J. 2003, *ApJ*, 584, 260
- Wiklind, T. A., Combes, F., & Henkel, C. 1995, *A&A*, 297, 643
- Wrobel, J. M., & Heeschen, D. S. 1988, *ApJ*, 335, 677
- Xilouris, E. M., Madden, S. C., Galliano, F., et al. 2004, *A&A*, 416, 41
- Young, L. M. 2002, *AJ* 124, 788

Young, L. M. 2005, ApJ 634, 258

Young, L. M., Bureau, M., & Cappellari, M. 2008, ApJ, 676, 317

Yun, M. S., Reddy, N. A., & Condon, J. J. 2001 ApJ 554, 803

Table 1. Sample Galaxies – Basic Properties

Name	RA (J2000.0)	Dec	Dist Mpc	Type	M_B	$(B - V)_e$	R_e "	σ_0 km s ⁻¹	M(H ₂) 10 ⁸ M _⊙	Refs.
UGC 1503	02 01 19.8	+33 19 46	71 (5)	E	-20.1	...	8	...	19 (3)	8
NGC 0807	02 04 55.7	+29 59 15	66 (5)	E	-20.8	0.97	12	175	14 (3)	8
NGC 2320	07 05 42.0	+50 34 42	84 (7)	E	-21.7	1.05	13	350	49 (7)	1, 2, 3
NGC 3032	09 52 08.2	+29 14 10	21.2 (1.9)	S0 ⁰	-18.8	0.63	12	82	4.9 (1.0)	4, 5
NGC 3656	11 23 38.4	+53 50 31	40 (3)	I0pec	-19.8	...	14	180	37 (5)	8
NGC 4459	12 29 00.0	+13 58 43	16.1 (0.4)	S0 ⁺	-20.0	0.97	25	174	1.7 (0.3)	6
NGC 4476	12 29 59.2	+12 20 55	17.6 (0.6)	S0 ⁻	-18.3	0.85	10	53	1.0 (0.1)	6
NGC 4526	12 34 03.0	+07 41 57	17.3 (1.5)	S0 ⁰	-20.8	0.98	44	256	6.3 (1.1)	2, 4, 7
NGC 5666	14 33 09.1	+10 30 37	31 (2)	?	-18.7	0.86	6	...	4.5 (0.6)	8

Note. — Distance references - (1) Riess et al. (2004); (2) Reindl et al. (2005); (3) Prieto et al. (2006); (4) Tonry et al. (2001); (5) Jensen et al. (2003); (6) Mei et al. (2007); (7) Wang et al. (2006); (8) de Vaucouleurs et al. (1991). In the latter case, distances are calculated using the velocity relative to the galactic center of rest and $H_0 = 73 \pm 5$ km s⁻¹ Mpc⁻¹. The CO fluxes are taken from Young (2002, 2005) and Young et al. (2008), and H₂ masses use a CO-to-H₂ conversion factor of 3.0×10^{20} cm⁻² (K km s⁻¹)⁻¹ at the updated distances. Effective radii are the *J*-band half-light radii from the 2MASS extended source catalog; note that in the cases of NGC 2320, NGC 4459, and NGC 4476 those values are significantly lower than the effective radii quoted by de Vaucouleurs et al. (1991), which are 37'', 35'', and 18'' respectively. Other data are taken from NASA's Extragalactic Database (NED) and the Lyon Extragalactic Database (LEDa). The morphological type of NGC 5666 is uncertain, as discussed in the text.

Table 2. Radio Continuum Image Parameters

Galaxy	Beam "	noise mJy beam ⁻¹	Peak mJy beam ⁻¹	S/N	Ref.
UGC 1503	5.0×4.5	0.038	0.33	8.7	LY07
NGC 0807	10.9×8.8	0.056	0.27	4.8	LY07
NGC 2320	5.4×5.4	0.17	13.1	77	FIRST
NGC 3032	5.4×5.4	0.14	1.22	8.7	FIRST
NGC 3656	4.5×3.8	0.037	9.4	254	LY07
NGC 4459	5.4×5.4	0.15	0.86	5.7	FIRST
NGC 4476	4.5×4.5	0.17	< 0.5	< 3	LY07
NGC 4526	5.4×5.4	0.15	3.75	25	FIRST
NGC 5666	4.6×4.4	0.050	1.9	38	LY07

Note. — Columns 4 and 5 give the peak surface brightness and peak signal-to-noise ratio on the target galaxy. References: Lucero & Young (2007) (LY07) or the VLA FIRST survey (Becker, White, & Helfand 1995).

Table 3. MIPS Flux Densities and Color Temperatures

Galaxy	$S_{24\mu\text{m}}$ Jy	$S_{70\mu\text{m}}$ Jy	$S_{160\mu\text{m}}$ Jy	Color Temp. K
UGC 1503	0.0482 ± 0.0019	0.793 ± 0.079	1.49 ± 0.18	25.0 ± 0.7
NGC 0807	0.0689 ± 0.0028	0.608 ± 0.061	2.39 ± 0.29	22.2 ± 0.5
NGC 2320	0.0220 ± 0.0009	0.385 ± 0.077	1.12 ± 0.13	22.9 ± 0.5
NGC 3032	0.165 ± 0.007	2.66 ± 0.266	3.32 ± 0.40	27.6 ± 0.6
NGC 3656	0.169 ± 0.007	3.63 ± 0.36	3.81 ± 0.46	27.5 ± 0.8
NGC 4459	0.129 ± 0.005	3.10 ± 0.19	3.76 ± 0.45	27.1 ± 0.6
NGC 4476	0.0400 ± 0.0016	0.886 ± 0.133	1.38 ± 0.17	25.6 ± 0.7
NGC 4526	0.314 ± 0.013	10.2 ± 0.61	12.7 ± 1.5	26.5 ± 0.5
NGC 5666	0.162 ± 0.006	3.00 ± 0.30	2.48 ± 0.30	28.0 ± 0.8

Table 4. FIR and Radio Continuum Emission

Galaxy	$S_{350\mu\text{m}}$ Jy	$S_{100\mu\text{m}}$ Jy	$S_{60\mu\text{m}}$ Jy	$S_{1.4\text{GHz}}$ mJy	q
UGC 1503	0.24 ± 0.05	1.44 ± 0.15	0.50 ± 0.04	2.5 ± 0.5	2.57 ± 0.09
NGC 0807	0.45 ± 0.09	1.83 ± 0.12	0.41 ± 0.03	1.2 ± 0.4	2.91 ± 0.15
NGC 2320	...	1.60 ± 0.16	0.26 ± 0.02	19.3 ± 0.7	1.60 ± 0.03
NGC 3032	...	4.70 ± 0.47	1.94 ± 0.10	7.2 ± 0.5	2.66 ± 0.04
NGC 3656	0.69 ± 0.14	6.58 ± 0.66	2.54 ± 0.13	19.8 ± 0.7	2.35 ± 0.03
NGC 4459	...	4.82 ± 0.48	1.87 ± 0.09	1.8 ± 0.2	3.25 ± 0.05
NGC 4476	0.28 ± 0.06	1.84 ± 0.18	0.66 ± 0.05	< 0.5	> 3.38
NGC 4526	...	17.1 ± 1.7	5.56 ± 0.05	12.0 ± 0.5	2.94 ± 0.03
NGC 5666	0.52 ± 0.10	3.98 ± 0.40	1.99 ± 0.10	17.5 ± 0.7	2.24 ± 0.03

Note. — Flux densities at $350\mu\text{m}$ are taken from Leeuw et al. (2008). *IRAS* $60\mu\text{m}$ and $100\mu\text{m}$ flux densities are taken from the 1994 communication of Knapp as tabulated in NED. The 20cm radio continuum fluxes are from the NRAO VLA Sky Survey (NVSS; Condon et al. 1998) for the five targets brightest at 20cm, and for NGC 4459 it is taken from the FIRST survey (Becker, White, & Helfand 1995). The remaining three have 20cm radio continuum flux densities from Lucero & Young (2007).

Table 5. Summary of Star Formation Evidence

Name	Resolved radio?	Spatial Correlations		Optical/UV	FIR/radio	Notes
		24 μ m vs. radio?	24 μ m vs. CO?			
UGC 1503	Y	Y	Y	...	Y	SF ring.
NGC 0807	Y	plateau/disk: Y pt src: No	Y No	...	Y	Some SF.
NGC 2320	No	No	No	...	No	No SF?
NGC 3032	Y	Y	Y	1, 2, 3	Y	SF inner disk.
NGC 3656	Y	Y	Y	...	Y	SF inner disk.
NGC 4459	No	2'' disk: Y 33'' disk: No	Y No	1,2	Y	SF inner disk.
NGC 4476	Y	4, 5	...	SF ring.
NGC 4526	Y	plateau: Y 28'' disk: No	Y No	1, 2	Y	SF inner disk.
NGC 5666	Y	Y	Y	6	Y	SF ring.

Note. — Column 2 refers to whether the cm-wave radio continuum emission is resolved on size scales (and orientations) similar to those of the molecular disk. Column 3 refers to whether the 24 μ m emission or its morphological sub-components have size scales similar to those of the radio continuum. Column 4 refers to whether the 24 μ m emission morphology matches that of the molecular gas (possibly being somewhat more compact than the molecular gas, if only part of the gas is forming stars). In column 5, references for the optical and UV star formation evidence are (1) Sarzi et al. (2005); (2) Kuntschner et al. (2006); (3) McDermid et al. (2006a); (4) this paper (Section 6.2.7); (5) Gil de Paz et al. (2007); (6) Donzelli & Davoust (2003). Column 6 lists whether the FIR/radio flux density ratios are consistent with star formation (Section 7.2).

Table 6. $24\mu\text{m}$ Fit Parameters

Parameter	Value
UGC 1503 (Ring)	
Total flux density	46.6 ± 1.3 mJy
Radius of maximum	$4.8'' \pm 0.4''$ (1.65 ± 0.14 kpc)
Outer scale length	$3.2'' \pm 0.2''$ (1.10 ± 0.07 kpc)
Inner scale length	$2.2'' \pm 0.6''$ (0.8 ± 0.2 kpc)
Axis ratio	0.73 ± 0.03
Position Angle	$58^\circ \pm 2^\circ$
NGC 0807 (Plateau, disk, and point source)	
Plateau outer scale	$3.77'' \pm 0.12''$ (1.21 ± 0.04 kpc)
Plateau axis ratio	0.423 ± 0.002
Plateau PA	$-37.57^\circ \pm 0.06^\circ$
Exp. disk flux density	31.23 ± 0.07 mJy
Exp. disk scale length	$16.99'' \pm 0.14''$ (5.44 ± 0.04 kpc)
Exp. disk axis ratio	0.577 ± 0.004
Exp. disk PA	$-40.2^\circ \pm 0.2^\circ$
Nuclear point source	3.36 ± 0.08 mJy
NGC 2320 ($r^{1/4}$ model)	
Total flux density	20 ± 2 mJy
Effective radius (major)	$4.06'' \pm 0.06''$ (1.65 ± 0.02 kpc)
Effective radius (minor)	$1.88'' \pm 0.06''$ (0.77 ± 0.2 kpc)
PA	$-37^\circ \pm 2^\circ$

Table 6—Continued

Parameter	Value
NGC 3032 (Exp. disk plus point source)	
Exp. disk flux density	140 ± 10 mJy
Exp. disk scale length	$1.83'' \pm 0.04''$ (0.188 ± 0.004 kpc)
Exp. disk axis ratio	0.808 ± 0.006
Exp. disk PA	$63^\circ \pm 6^\circ$
Off-nuclear point source ^a	6 ± 14 mJy
NGC 3656 (Exponential disk)	
Exp. disk flux density	146 ± 4 mJy
Exp. disk scale length	$2.0'' \pm 0.4''$ (0.39 ± 0.08 kpc)
Exp. disk axis ratio	0.30 ± 0.05
Exp. disk PA	$-5.7^\circ \pm 1.4^\circ$
NGC 4459 (Two exponentials)	
Disk 1 flux density	100 ± 1 mJy
Disk 1 scale length	$2.08'' \pm 0.02''$ (0.162 ± 0.001 kpc)
Disk 1 axis ratio	0.706 ± 0.006
Disk 1 PA	$-75.3^\circ \pm 0.7^\circ$
Disk 2 flux density	29 ± 5 mJy
Disk 2 scale length	$33'' \pm 8''$ (2.6 ± 0.6 kpc)
Disk 2 axis ratio	0.85 ± 0.03
Disk 2 PA	$-44^\circ \pm 2^\circ$
NGC 4476 (Ring plus point source)	
Ring total flux density	31.6 ± 0.2 mJy
Radius of maximum	$6.0'' \pm 0.2''$ (0.51 ± 0.02 kpc)

Table 6—Continued

Parameter	Value
Outer scale length	$1.29'' \pm 0.07''$ (0.110 ± 0.006 kpc)
Inner scale length	$3.7'' \pm 0.6''$ (0.32 ± 0.05 kpc)
Axis ratio	0.447 ± 0.009
PA	$24.5^\circ \pm 0.6^\circ$
Off-nuclear point source ^a	5 ± 2 mJy
NGC 4526 (Plateau plus exponential disk)	
Plateau total flux density	254 ± 1 mJy
Plateau radius	$7.5'' \pm 0.1''$ (0.629 ± 0.003 kpc)
Outer scale length	$1.91 \pm 0.06''$ (0.160 ± 0.005 kpc)
Axis ratio	0.20099 ± 0.00017
PA	$-68.46^\circ \pm 0.14^\circ$
Exp. disk flux density	54.0 ± 0.6 mJy
Scale length	$28.4'' \pm 1.2''$ (2.4 ± 0.1 kpc)
Axis ratio	0.397 ± 0.004
PA	$-71^\circ \pm 0.4^\circ$
NGC 5666 (Plateau)	
Total flux density	144 ± 3 mJy
Plateau radius	$5.87'' \pm 0.12''$ (0.88 ± 0.02 kpc)
Outer scale length	$0.5'' \pm 0.4''$ (0.08 ± 0.06 kpc)
Axis ratio	0.86 ± 0.26
PA	$-49^\circ \pm 28^\circ$

^aAs the point source in NGC 3032 is weak and is $8''$ from the galaxy center it may be a background source. Similarly, the point source in NGC 4476 is $6''$ northeast of the nucleus and has the effect of making that ansa brighter, but it may also be a background source.

Table 7. Star Formation Rates and Depletion Timescales

Galaxy	$\log L(24\mu\text{m})$ erg s ⁻¹	SFR M _⊙ yr ⁻¹	τ_{gas} 10 ⁹ yr
UGC 1503	42.57	0.60	4.3
NGC 0807	42.66	0.69	2.7
NGC 2320	42.37	< 0.40	> 17
NGC 3032	42.05	0.21	3.2
NGC 3656	42.61	0.66	7.7
NGC 4459	41.71	0.083	2.8
NGC 4476	41.27	0.043	3.2
NGC 4526	42.15	0.22	4.0
NGC 5666	42.37	0.40	1.5

Note. — For NGC 2320 the star formation rate is an upper limit because we have argued that the bulk of the 24 μm emission does not arise in star formation in this galaxy. For NGC 4459 and NGC 4526 we have argued that only $\approx 80\%$ of the 24 μm emission should be attributed to star formation and the star formation rate reflects that attribution. For NGC 807 we have argued that somewhere between 50% and 95% of the 24 μm emission is driven by star formation activity but the quoted star formation rate uses the higher value.

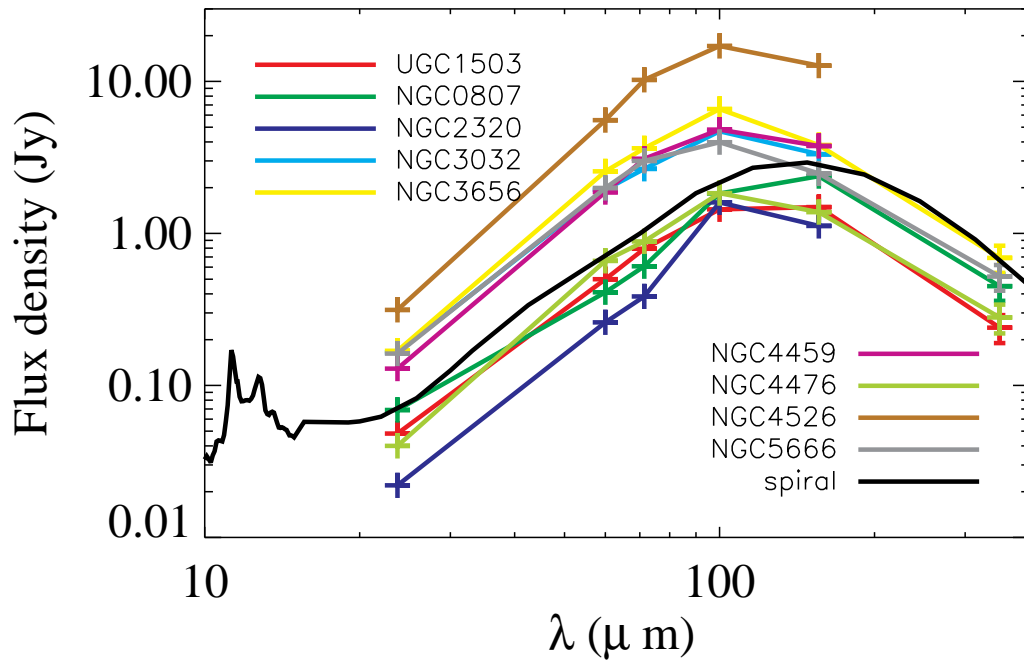


Fig. 1.— Mid- and far-IR flux densities for the CO-rich early-type galaxy sample. The $350\mu\text{m}$ points are plotted with appropriate error bars; at wavelengths shorter than $350\mu\text{m}$, uncertainties are estimated at 5% to 20% (see text) so are comparable to or smaller than the symbol size. The SED of a “typical spiral” galaxy, from Dale et al. (2007), is overlaid.

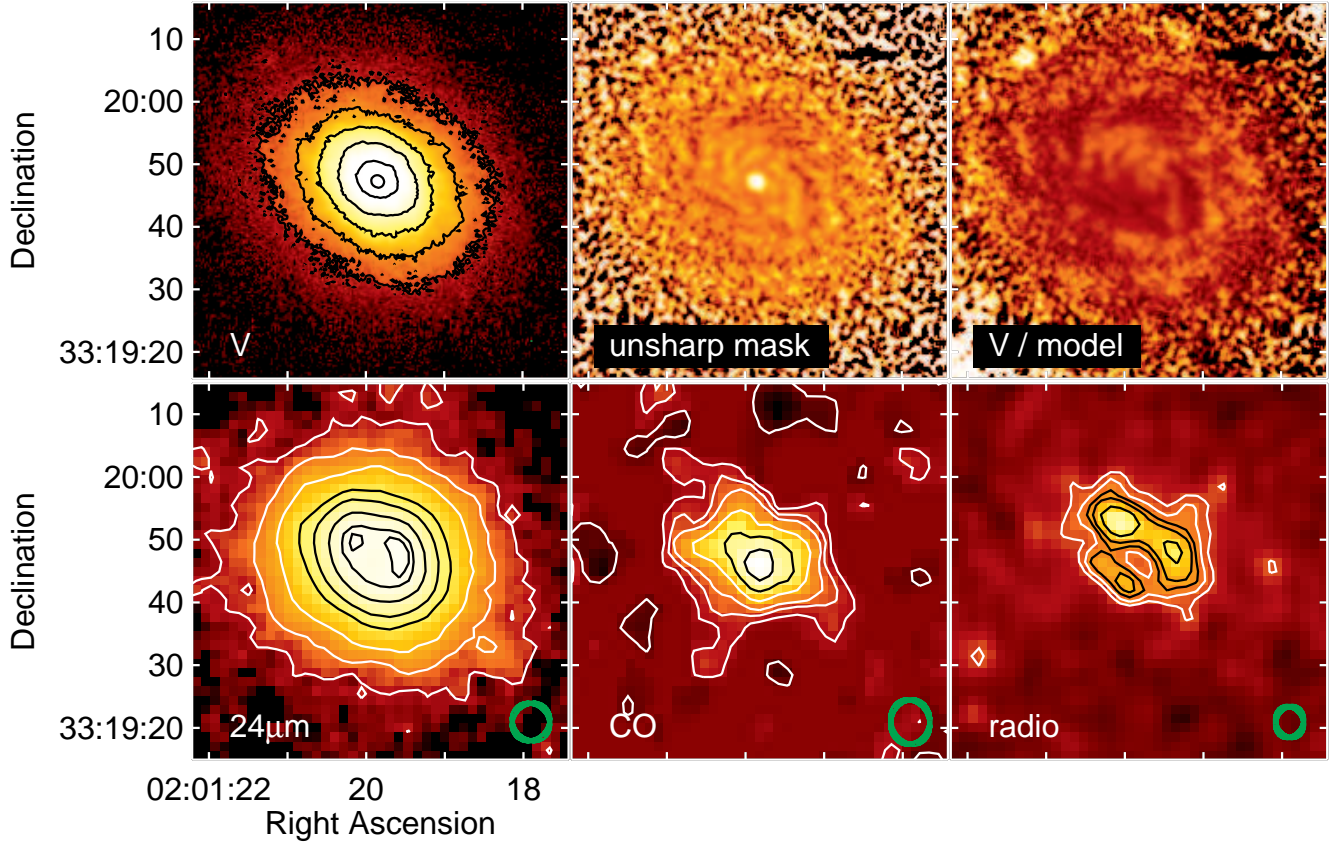


Fig. 2.— Optical, IR, CO and radio continuum morphology of UGC 1503. Optical contours are spaced by a factor of two. A $V - R$ image shows no discernible structure but the unsharp masking and model division techniques do show some faint structure. Contour levels in the $24\mu\text{m}$ image are 0.12, 0.31, 0.61, 1.22, 1.83, 3.05, 4.27, and 4.70 MJy sr^{-1} (the lowest three are 4.4σ , 11σ , and 22σ). Contour levels in the CO image are -0.63 , 0.63, 1.27, 1.90, 3.12, 4.43, and $5.70 \text{ Jy b}^{-1} \text{ km s}^{-1}$. Contours in the 1.4 GHz radio continuum image are 0.09, 0.12, 0.15, 0.18, and $0.24 \text{ mJy beam}^{-1}$ (2.4 , 3.1 , 3.9 , 4.7 , and 6.3σ). In this and subsequent figures, green circles in the lower right corners of panels indicate the resolution (FWHM) of their respective data. Contours are colored either white or black as necessary to enhance their visibility.

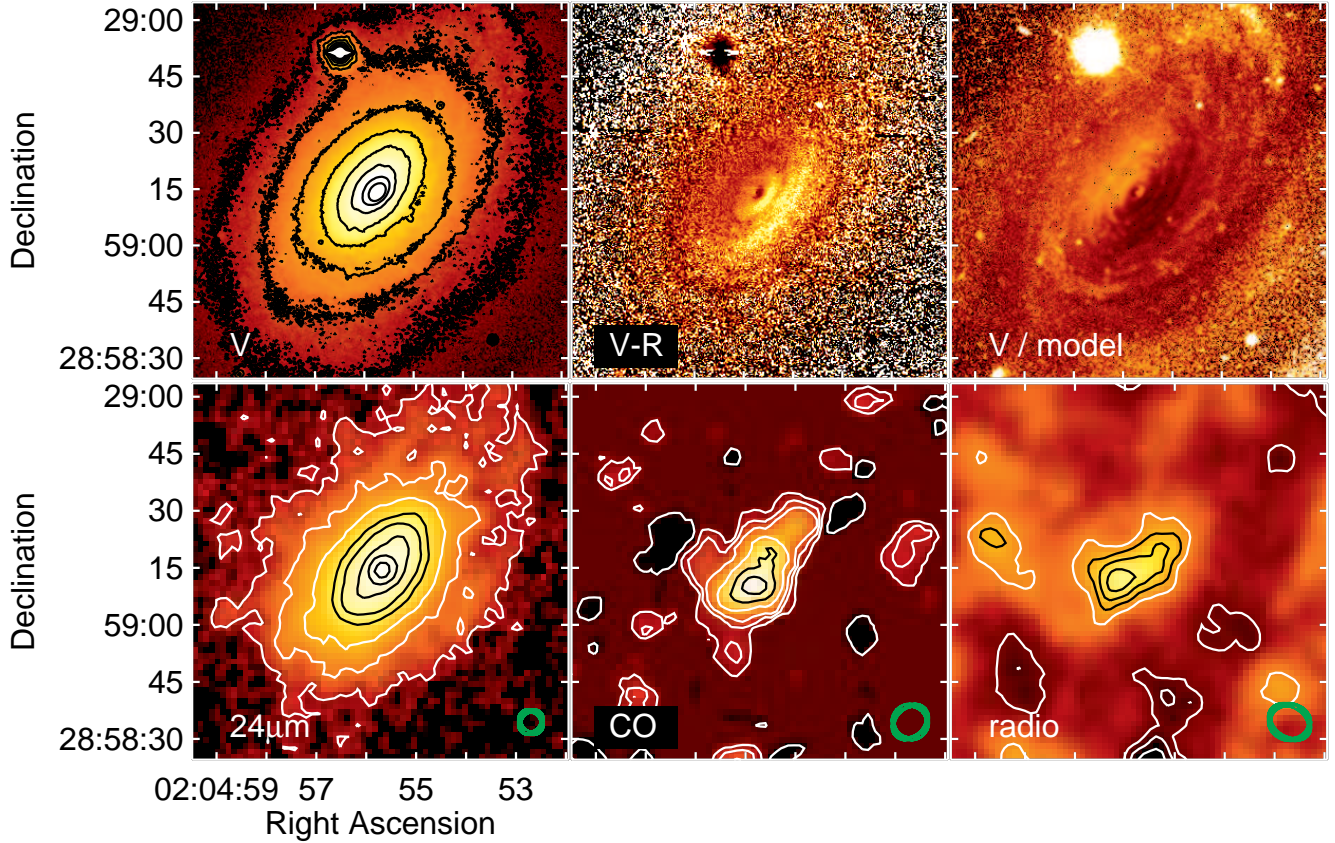


Fig. 3.— Optical, IR, CO and radio continuum morphology of NGC 807. Optical contours are spaced by a factor of two. The top row, middle panel is a $V - R$ image and the top row, right panel is a V image divided by a smooth MGE model constructed using the software of Cappellari (2002). Contours in the $24\mu\text{m}$ image are 0.12, 0.29, 0.58, 1.16, 1.74, 2.91, 4.07, and 5.23 MJy sr^{-1} (the lowest three are 4.3σ , 10σ , and 20σ). Contours in the CO image are -0.77 , 0.77 , 1.53 , 2.30 , 3.83 , 5.33 , and $6.88 \text{ Jy b}^{-1} \text{ km s}^{-1}$. Contours in the 1.4 GHz radio continuum image are -0.2 , -0.15 , -0.1 , 0.1 , 0.15 , 0.2 , and $0.25 \text{ mJy beam}^{-1}$ (-3.6 , -2.7 , -1.8 , 1.8 , 2.7 , 3.6 , and 4.5σ).

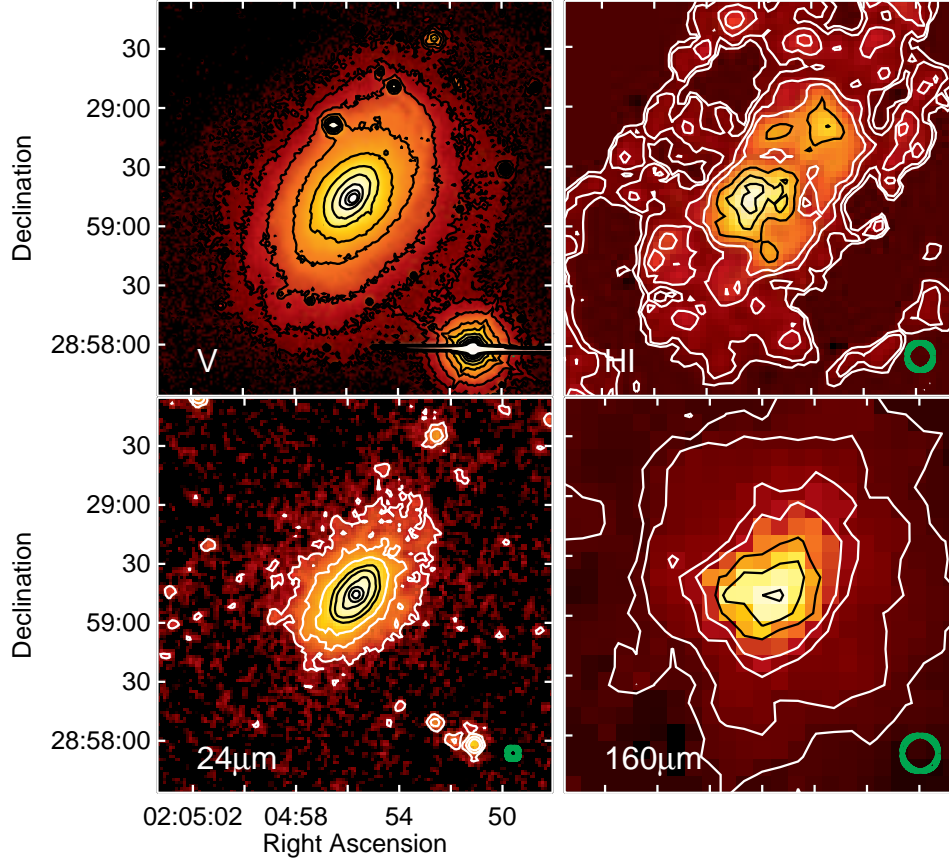


Fig. 4.— Large-scale optical, IR, and HI morphology of NGC 807. Optical contours are spaced by a factor of two. Contour levels in the $24\mu\text{m}$ image are the same as in Figure 3. Contour levels in the $160\mu\text{m}$ image are 1.14, 2.28, 4.56, 6.84, 11.4, 16.0, and 20.5 MJy sr^{-1} (the lowest three are 2.0σ , 4.1σ , and 8.2σ). The HI integrated intensity image has a resolution of $14'' \times 13''$ and contour levels are at 0.01, 0.02, 0.04, 0.06, 0.10, 0.14, and $0.18 \text{ Jy b}^{-1} \text{ km s}^{-1}$, where the peak in the HI intensity is $0.20 \text{ Jy b}^{-1} \text{ km s}^{-1} = 1.2 \times 10^{21} \text{ cm}^{-2}$.

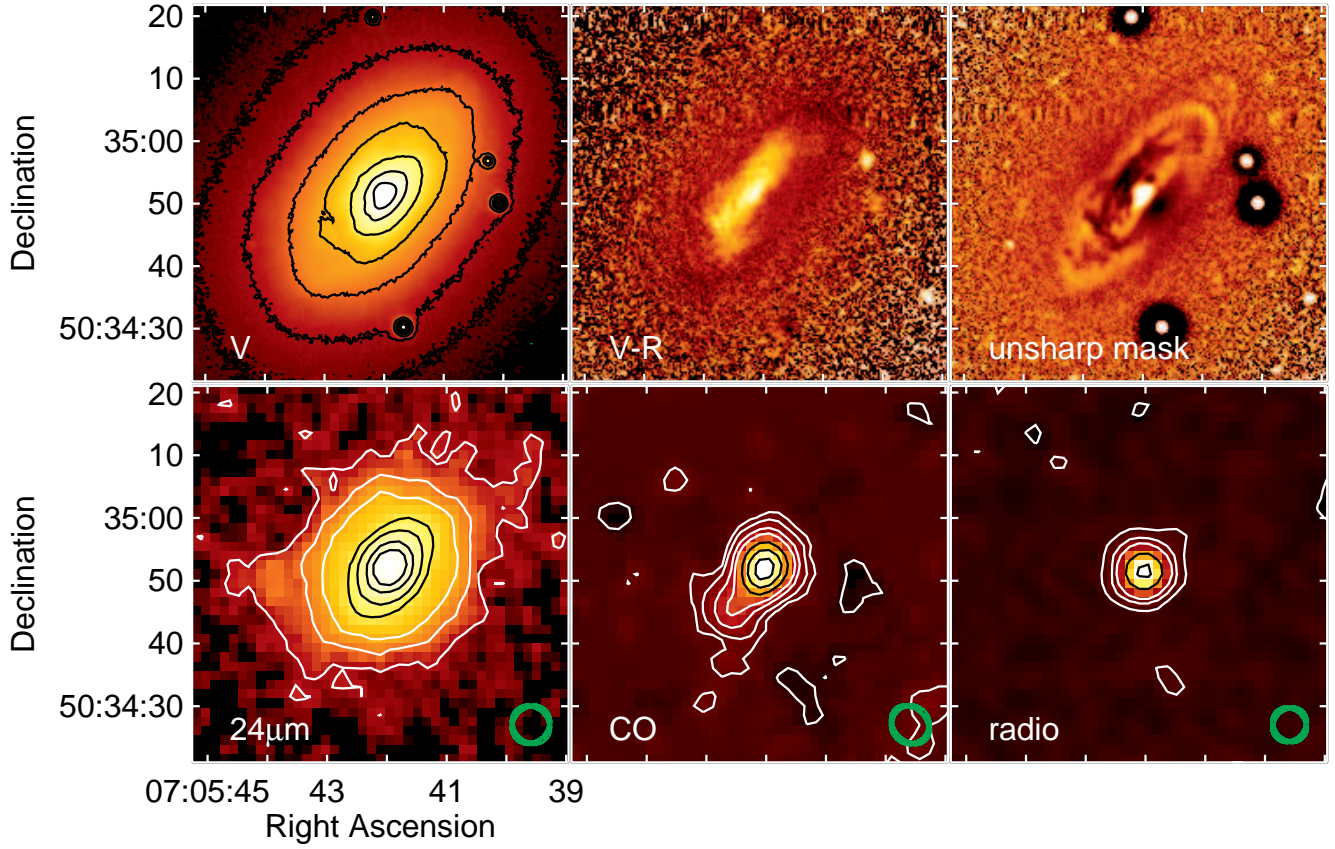


Fig. 5.— Optical, IR, CO and radio continuum morphology of NGC 2320. Optical contours are spaced by a factor of two. Contours in the $24\mu\text{m}$ image are 0.11, 0.28, 0.56, 1.13, 1.69, 2.82, 3.94, and 5.08 MJy sr^{-1} (the lowest three are 3.9σ , 9.8σ , and 20σ). Contours in the CO image are -1.46 , 1.46, 2.91, 5.82, 8.73, 14.5, 20.4, and $26.2 \text{ Jy b}^{-1} \text{ km s}^{-1}$. Contours in the 1.4 GHz radio continuum image are -0.39 , 0.39, 1.31, 2.62, 6.55, and $11.8 \text{ mJy beam}^{-1}$ (-2.3 , 2.3, 7.7, 15, 39, and 69σ).

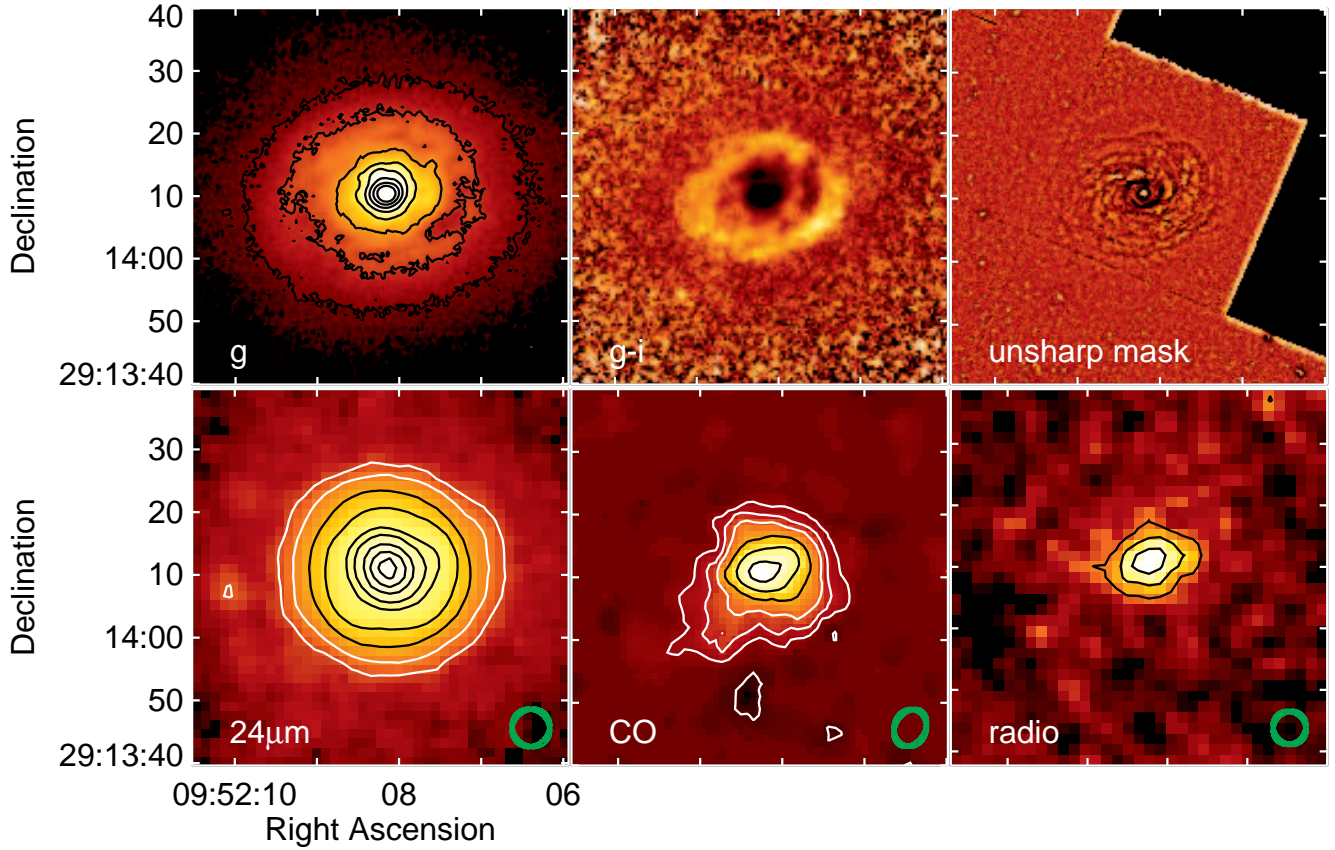


Fig. 6.— Optical, IR, CO and radio continuum morphology of NGC 3032. Optical contours are spaced by a factor of two. The unsharp-masked image is from a WFPC2 F606W image. Contours in the $24\mu\text{m}$ image are 0.51, 1.01, 2.53, 5.06, 10.1, 15.2, 25.3, 35.4, and 45.5 MJy sr^{-1} (the lowest three are 16σ , 32σ , and 81σ). Contours in the CO image are -1.81 , 1.81 , 3.62 , 5.43 , 9.05 , 12.7 , and $16.3 \text{ Jy b}^{-1} \text{ km s}^{-1}$. Contours in the 1.4 GHz radio continuum image are 3.2, 5.4, and 7.5 times the rms noise level ($0.14 \text{ mJy beam}^{-1}$).

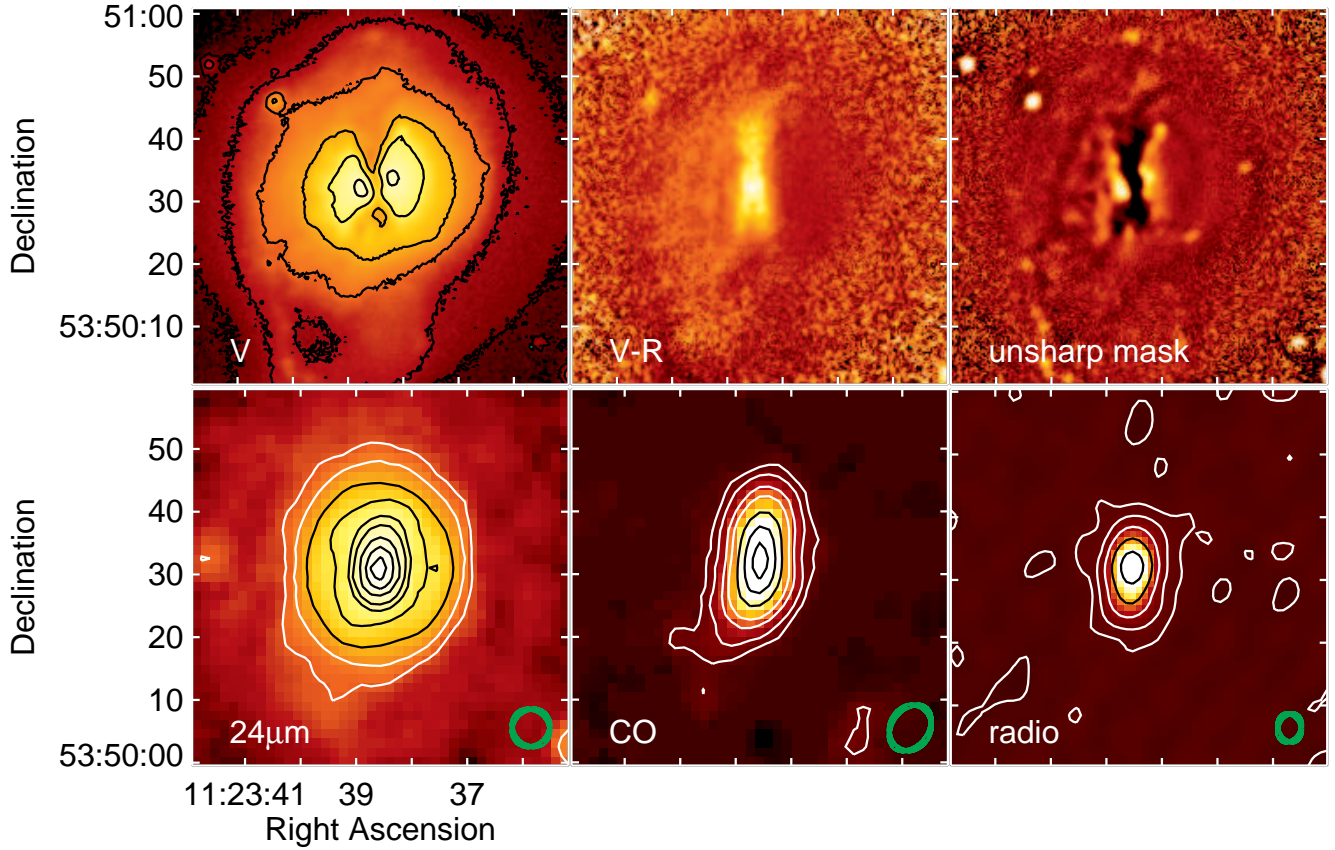


Fig. 7.— Optical (V), IR, CO and radio continuum morphology of NGC 3656. Optical contours are spaced by a factor of two. The unsharp-masked image is made from the V image. Contours in the $24\mu\text{m}$ image are 0.57, 1.15, 2.87, 5.75, 11.5, 17.2, 28.7, 40.2, and 51.7 MJy sr^{-1} (the lowest two are 23σ and 26σ). Contours in the CO image are 4.05, 8.09, 16.2, 24.3, 40.5, 56.6, and 72.8 $\text{Jy b}^{-1} \text{km s}^{-1}$. Contours in the 1.4 GHz radio continuum image are -0.09 , 0.09, 0.3, 0.9, 2.4, and 6.0 mJy beam^{-1} (-2.4 , 2.4, 8.1, 24, 64, and 162σ).

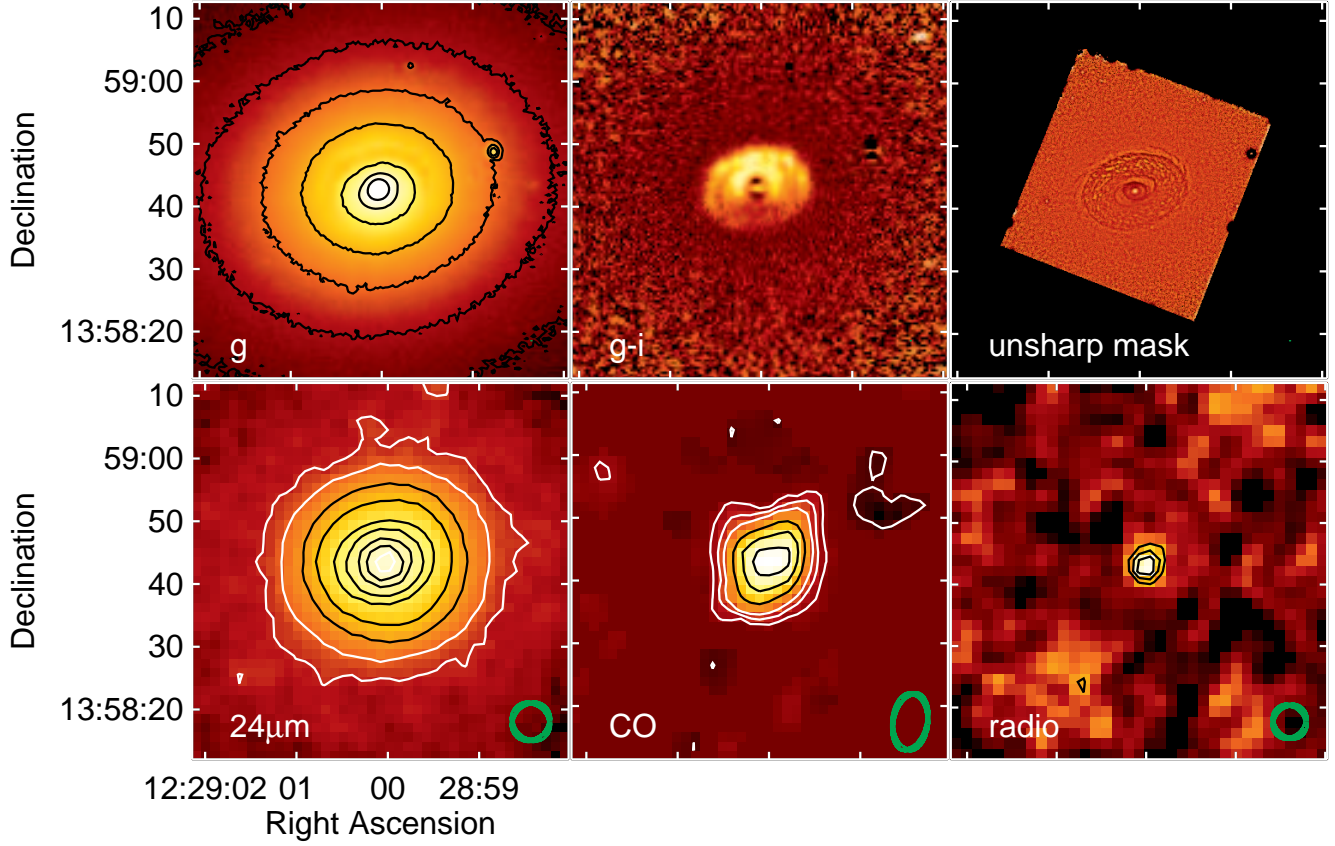


Fig. 8.— Optical, IR, CO and radio continuum morphology of NGC 4459. Optical contours are spaced by a factor of two. Contours in the $24\mu\text{m}$ image are 0.33, 0.66, 1.65, 3.30, 6.59, 9.89, 16.5, 23.1, and 29.7 MJy sr^{-1} (the lowest three are 8σ , 15σ , and 39σ). Contours in the CO image are -2.14 , 2.14 , 4.28 , 6.42 , 10.7 , 15.0 , and $19.3 \text{ Jy b}^{-1} \text{ km s}^{-1}$. Contours in the 1.4 GHz radio continuum image are -3 , 3 , 4 , and 5 times the rms noise level ($0.15 \text{ mJy beam}^{-1}$).

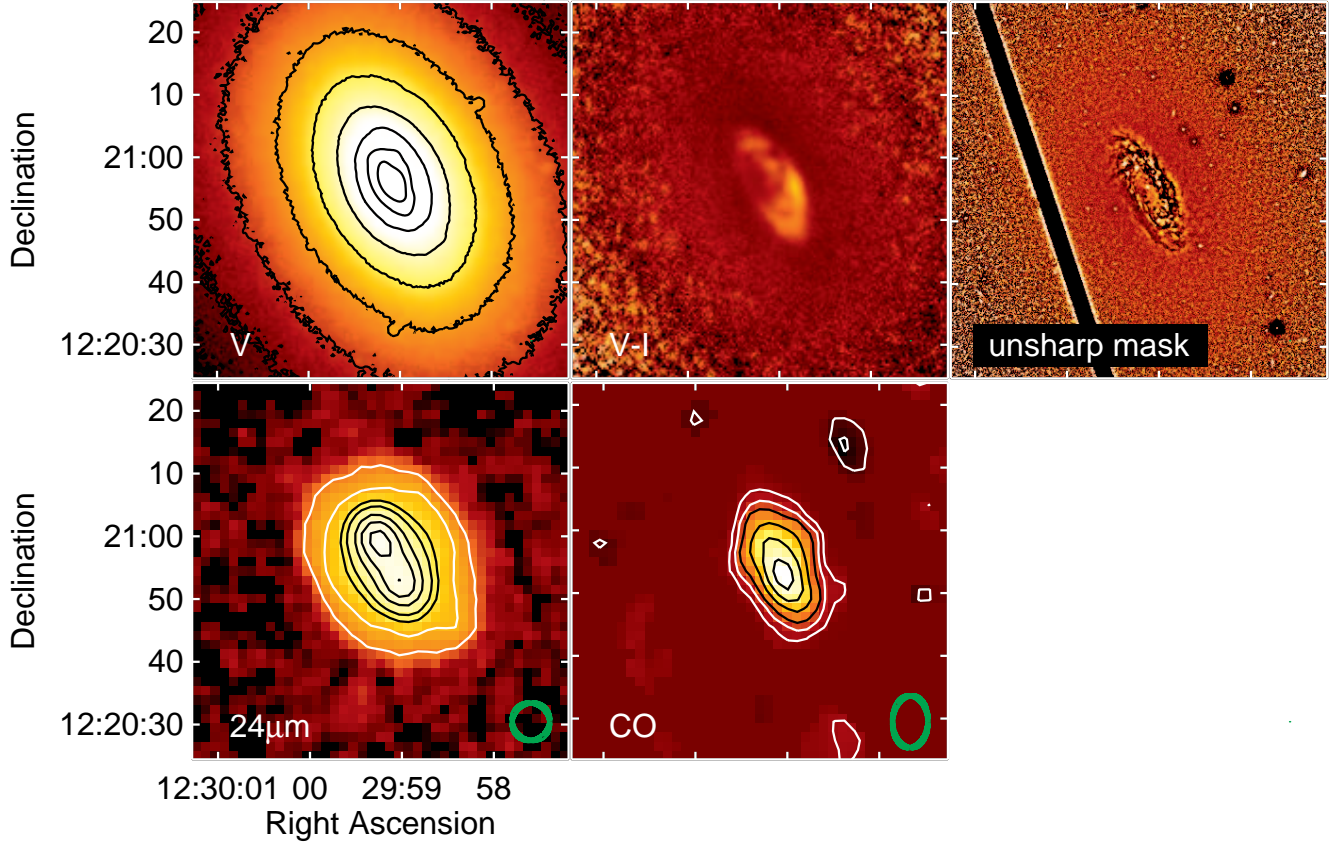


Fig. 9.— Optical, IR, CO and radio continuum morphology of NGC 4476. Optical contours are spaced by a factor of two. Contours in the $24\mu\text{m}$ image are 0.40, 0.80, 1.60, 2.40, 4.0, 5.6, and 7.2 MJy sr^{-1} (the lowest three are 13σ , 25σ , and 50σ). Contours in the CO image are -2.48 , -1.24 , 1.24 , 2.48 , 3.72 , 6.20 , 8.68 , and $11.2 \text{ Jy b}^{-1} \text{ km s}^{-1}$. Radio continuum emission from NGC 4476 is undetected (Lucero & Young 2007).

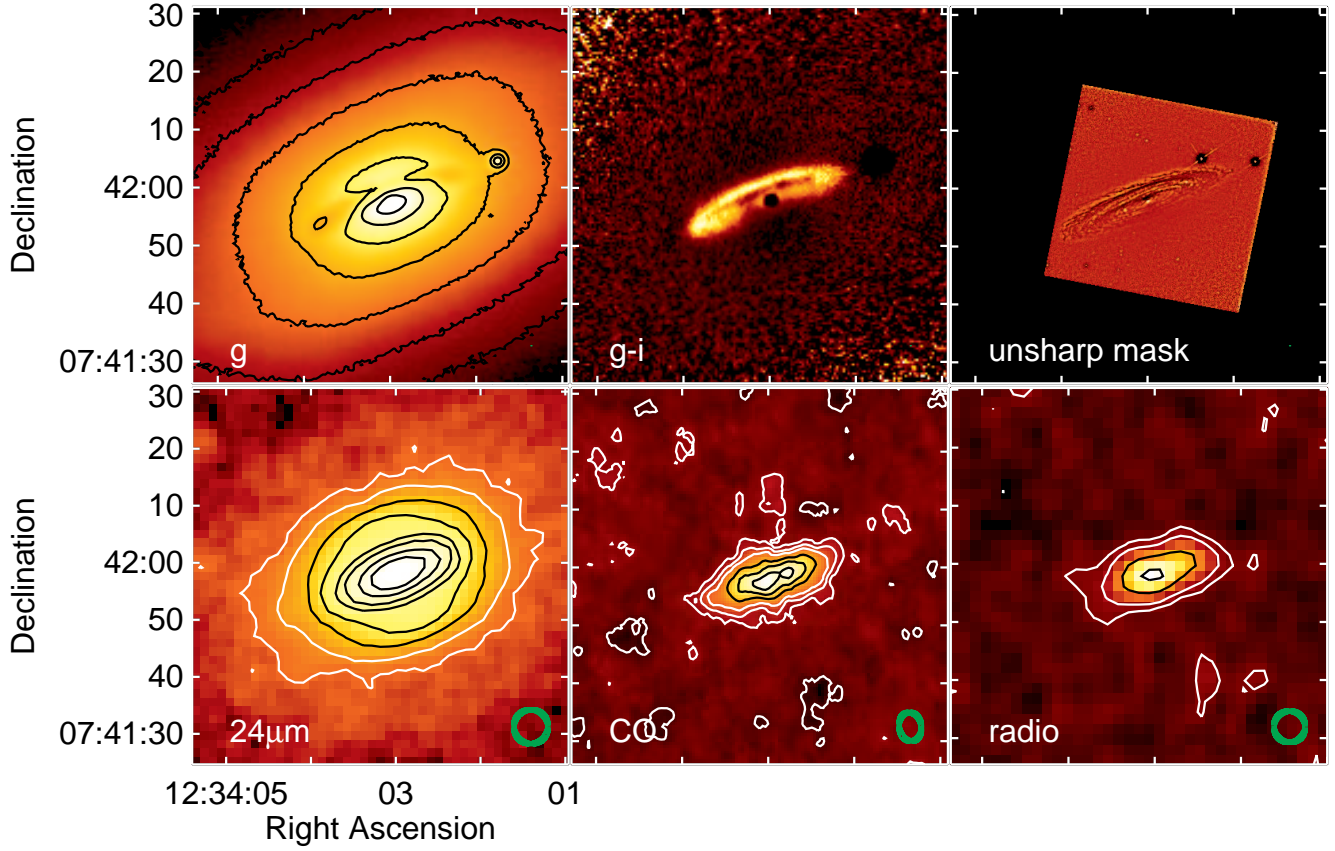


Fig. 10.— Optical, IR, CO and radio continuum morphology of NGC 4526. Optical contours are spaced by a factor of two. Contours in the $24\mu\text{m}$ image are 0.69, 1.38, 3.45, 6.90, 13.8, 20.7, 34.5, 48.3, and 62.1 MJy sr^{-1} (the lowest three are 7σ , 15σ , and 37σ). Contours in the CO image are -3.71 , 3.71, 7.42, 11.1, 18.6, 26.0, and $33.4 \text{ Jy b}^{-1} \text{ km s}^{-1}$. Contours in the 1.4 GHz radio continuum image are -0.38 , 0.38, 0.75, 1.88, and $3.37 \text{ mJy beam}^{-1}$ (-2.5 , 2.5, 5.0, 12.5, and 22σ).

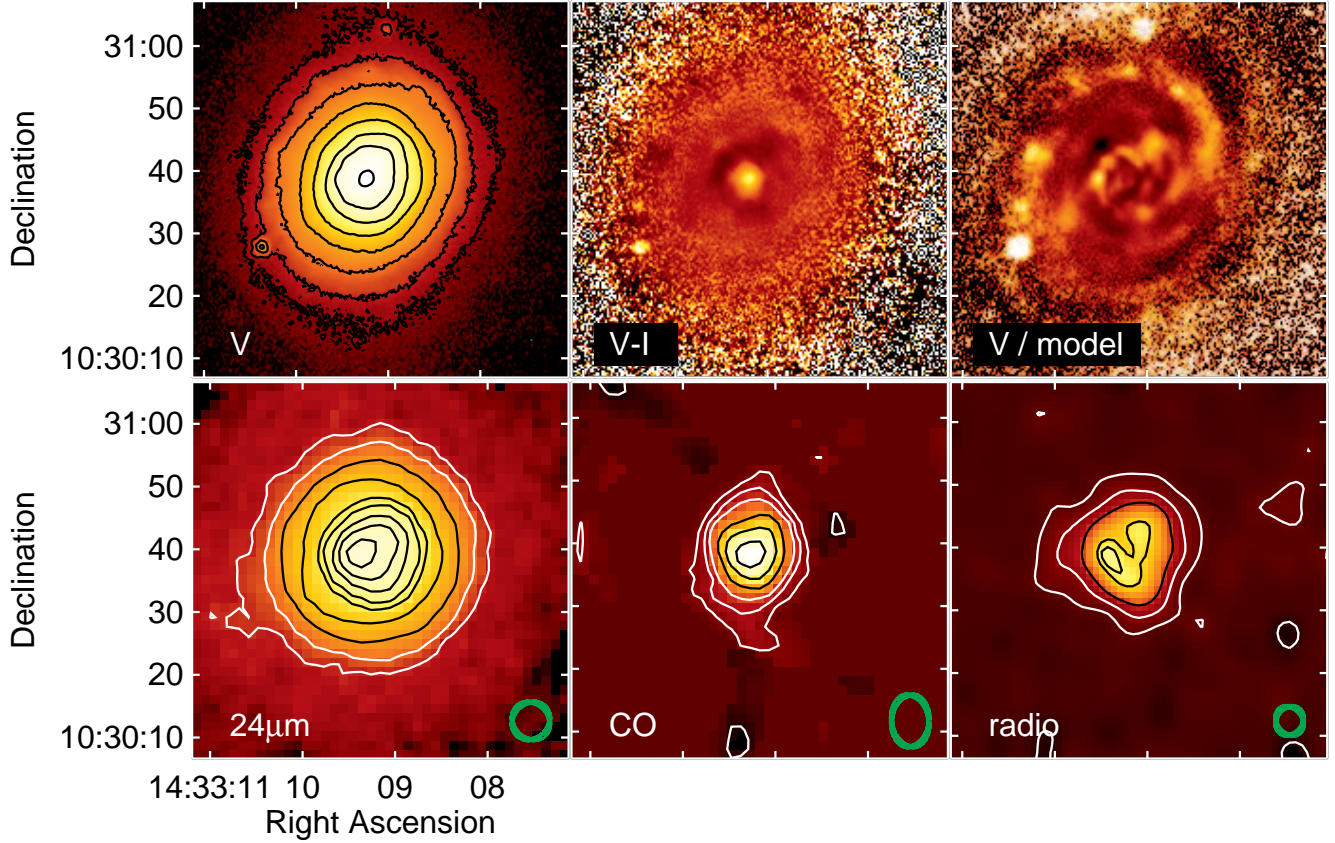


Fig. 11.— Optical, IR, CO and radio continuum morphology of NGC 5666. Optical contours are spaced by a factor of two. The top right panel is constructed by dividing the V image with a smooth elliptical MGE model. Contours in the $24\mu\text{m}$ image are 0.33, 0.67, 1.66, 3.33, 6.66, 9.99, 16.7, 23.3, and 30.0 MJy sr^{-1} (the lowest three are 12σ , 24σ , and 58σ). Contours in the CO image are -1.68 , 1.68, 3.35, 5.03, 8.38, 11.7, and $15.1 \text{ Jy b}^{-1} \text{ km s}^{-1}$. Contours in the radio continuum image are -0.12 , 0.12, 0.4, 0.8, 1.6, and $1.8 \text{ mJy beam}^{-1}$ (-2.4 , 2.4, 8, 16, 32, and 36σ).

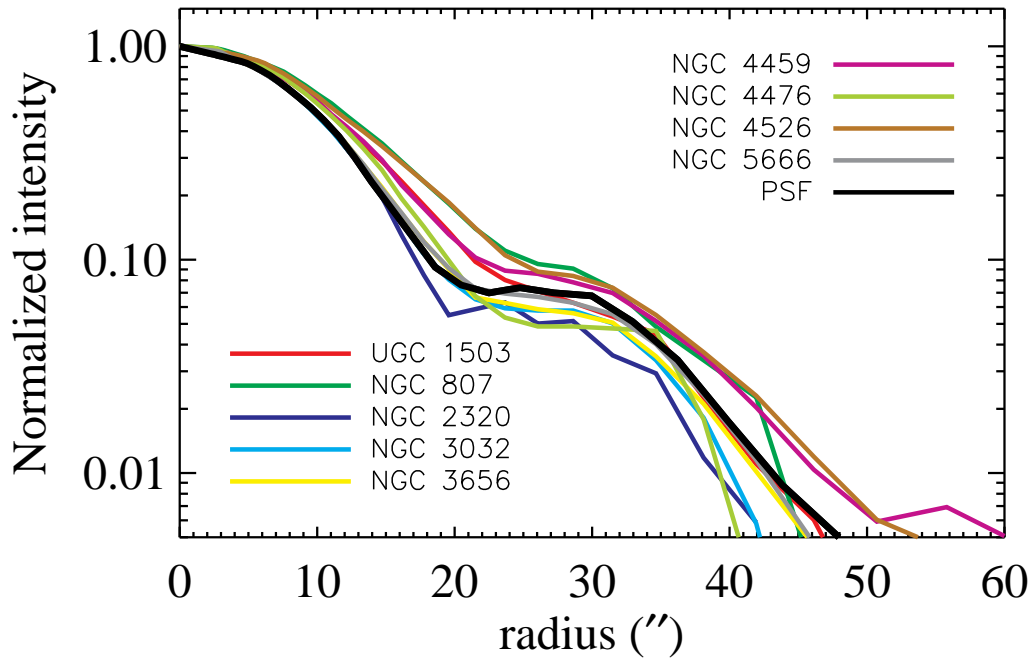


Fig. 12.— Surface brightness profiles at $70\mu\text{m}$, normalized to 1.0 at the center. Uncertainties in the surface brightness due to the rms pixel-to-pixel noise are at the level of a few percent near the first Airy minimum ($20''$) and rise to 10% in the radial range $40''$ to $60''$.

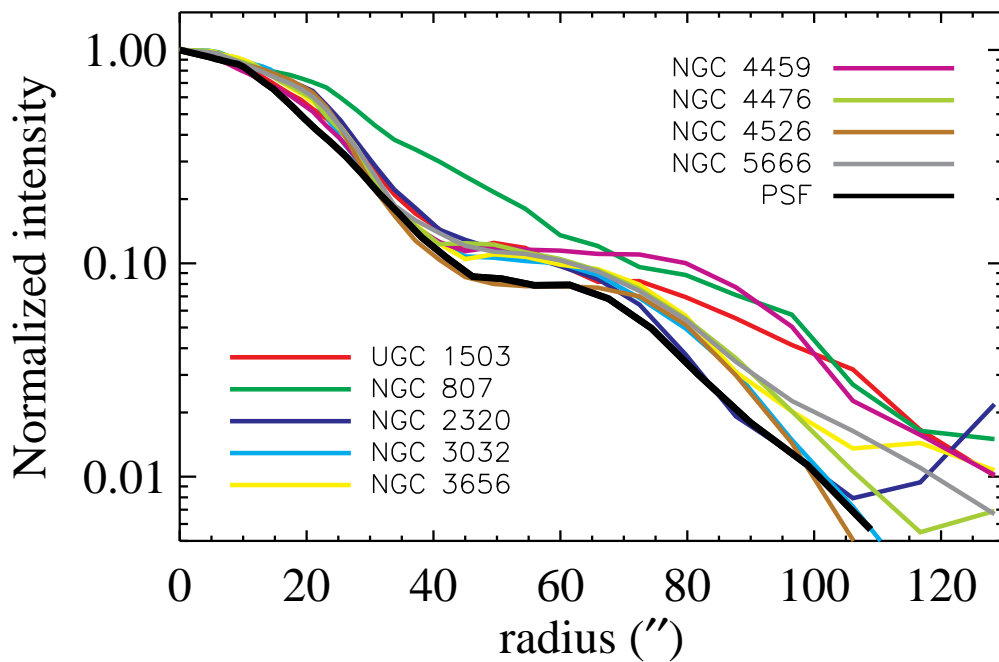


Fig. 13.— Surface brightness profiles at $160\mu\text{m}$. Uncertainties in the surface brightness are a few percent for radii $20''$ to $40''$ and are $\gtrsim 10\%$ at radii of $70''$ to $120''$, depending on the surface brightness.

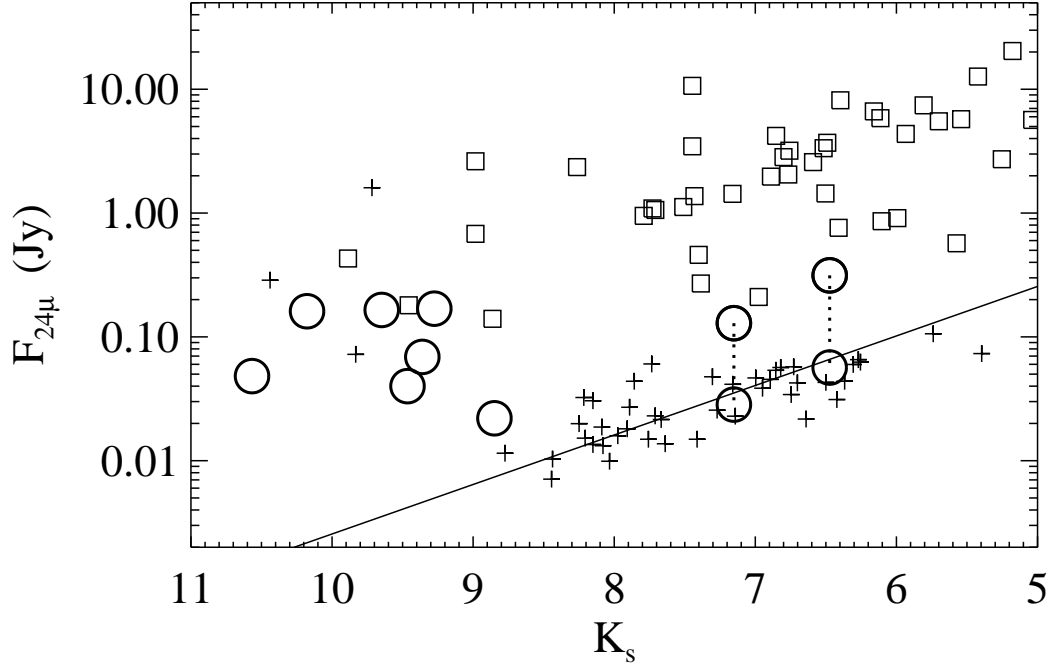


Fig. 14.— The $24\mu\text{m}$ flux density and K_s apparent magnitude for the CO-rich early-type galaxies (circles). For comparison, the sample of ellipticals studied by Temi et al. (2007) are shown as crosses and spirals from the SINGS sample are shown as squares (Dale et al. 2007). In addition, for NGC 4459 and NGC 4526 we show both the total $24\mu\text{m}$ flux density and the more extended component by itself, with dotted lines connecting the symbols. Uncertainties are comparable to or smaller than the symbol sizes. The solid line is not a fit but is instead a representative linear relationship between the $24\mu\text{m}$ and K_s flux density. In the generally CO-poor ellipticals of Temi et al. (2007), the $24\mu\text{m}$ emission is thought to be primarily associated with mass loss from the evolved stars. The extended $24\mu\text{m}$ components in NGC 4459 and NGC 4526 have $24\mu\text{m}/K_s$ ratios consistent with this behavior.

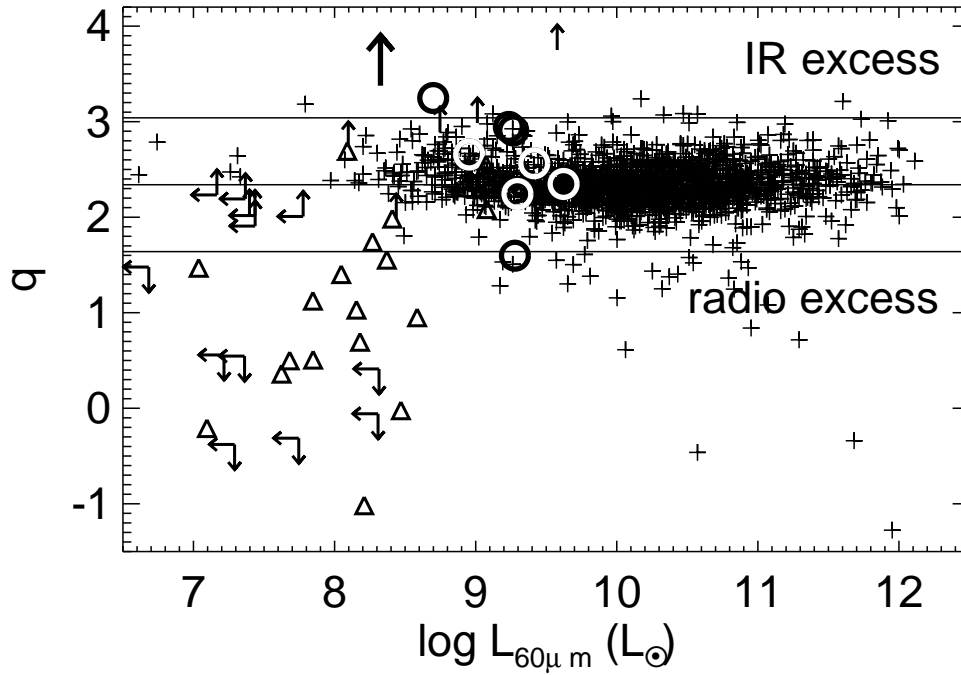


Fig. 15.— FIR-to-radio flux density ratio q . The circles and the large arrow are the CO-rich early-type galaxies studied here, and crosses are the data of Yun, Reddy, & Condon (2001). As defined by those authors, the flux ratio q has a mean value of 2.34 for star-forming galaxies (mostly spirals); the lines at $q = 3.04$ and $q = 1.64$ indicate the IR excess and radio excess boundaries, respectively, at roughly 2.7σ from the mean. Uncertainties are comparable to or smaller than the symbol sizes, though we have not included the effect of the distance uncertainty on the $60\mu\text{m}$ luminosity. The ratio q is, of course, independent of distance. Evidently the CO-rich early-type galaxies follow the same radio/FIR relation as the star forming spirals. Another sample of 48 elliptical galaxies from Temi et al. (2007) are shown in triangles and small arrows.